Research Square

Preprints are preliminary reports that have not undergone peer review.
They should not be considered conclusive, used to inform clinical practice,
or referenced by the media as validated information.

Biofilm-mediated disruption of wound repair signaling in Chronic Diabetic Foot Ulcer

Maria Infant Majula Shifani Mahendran
MGM Advanced Research Institute, Sri Balaji Vidyapeeth (Deemed to be University)
Vinoj Gopalakrishnan
vinojvino@gmail.com
MGM Advanced Research Institute, Sri Balaji Vidyapeeth (Deemed to be University)
Vaijayanthi Saravanan
MGM Advanced Research Institute, Sri Balaji Vidyapeeth (Deemed to be University)
Pradeep Jothimani
MGM Advanced Research Institute, Sri Balaji Vidyapeeth (Deemed to be University)
Siva Sakthi Srikanth
MGM Advanced Research Institute, Sri Balaji Vidyapeeth (Deemed to be University)
Carlos Henrique Gomes Martins
Federal University of Uberlândia

Research Article

Keywords: Diabetic Foot Ulcer, microbiome, 16S rRNA sequencing, biofilm, antimicrobial resistance, inflammation, and wound healing

Posted Date: November 16th, 2026

DOI: https://doi.org/10.21203/rs.3.rs-11477949/v1

License: This work is licensed under a Creative Commons Attribution 4.0 International License.
Read Full License

Additional Declarations: No competing interests reported.

Biofilm-mediated disruption of wound repair signaling in Chronic Diabetic Foot Ulcer

Maria Infant Majula Shifani[1], Vinoj Gopalakrishnan[1]*, Vaijayanthi Sarvanan[1], Pradeep Jothimani[1], Siva Sakthi Srikanth[1], Carlos Henrique Gomes Martins[2]

[1]*MGM Advanced Research Institute, Sri Balaji Vidyapeeth (Deemed to be University), Pondicherry-607402, India.*

[2]*Laboratory of Antimicrobial Testing, Institute of Biomedical Sciences, Federal University of Uberlândia, Uberlândia, Minas Gerais 38405-320, Brazil.*

[*]***e-mail: vinojvino@gmail.com***

Contact number: +91 97916 09004

Address: MGM Advanced Research Institute, SBV campus, Pillayarkuppam, Pondicherry- 607402, India.

Abstract

Background: Diabetic foot ulcers are chronic wounds in which infection, impaired tissue repair, and vascular abnormalities contribute to progressive tissue destruction and amputation. This study characterized microbial composition and host tissue alterations in ulcers requiring amputation. Materials and Methods: Of 135 clinically evaluated patients with diabetic foot ulcers, five undergoing amputation were included for deep-tissue analysis. Bacterial communities were characterized using 16S rRNA V3–V4 metagenomic sequencing. Clinically relevant bacterial isolates were evaluated for antimicrobial susceptibility and biofilm formation. Histopathology assessed tissue injury and vascular alterations, while quantitative gene-expression analysis evaluated inflammatory, fibroblast-associated, extracellular-matrix-remodeling, and collagen-related markers. Results: Deep-tissue sequencing revealed heterogeneous bacterial communities dominated by Proteobacteria, Actinobacteriota, Firmicutes, and Bacteroidota. Predominant genera included *Corynebacterium, Acinetobacter, Porphyromonas, Escherichia–Shigella, Veillonella,* and *Streptococcus*. Anaerobic taxa included *Porphyromonas, Prevotella, Parvimonas, Anaerococcus, Atopobium, Fusobacterium,* and *Solobacterium*. Isolates exhibited multidrug-resistant phenotypes. Histopathology demonstrated ulceration, inflammatory-cell infiltration, necrosis, fibrocollagenous tissue damage, and vascular abnormalities. Diabetic foot ulcer tissues showed increased expression of IL-8, IL-2, MMP1, S100A4, ACTA2, and COL3A1, whereas COL1A1 was reduced. *A. baumannii, S. aureus,* and *S. moorei* demonstrated time-dependent biofilm formation. Notably, *S. moorei* biofilm formation suggests potential persistence in advanced diabetic foot ulcers and warrants further investigation of its role in impaired wound repair. **Conclusion:** Severe amputation-associated diabetic foot ulcers exhibit heterogeneous polymicrobial communities. These ulcers also exhibit multidrug-resistant and biofilm-forming bacteria, extensive tissue injury, and dysregulated host repair responses. These convergent microbial and host abnormalities may sustain tissue destruction and non-healing. Supporting integrated strategies targeting infection, biofilms, and impaired tissue repair.

Keywords: Diabetic Foot Ulcer; microbiome; 16S rRNA sequencing; biofilm; antimicrobial resistance; inflammation; and wound healing.

1. Introduction

DFUs are among the most serious and debilitating complications of diabetes mellitus and are associated with prolonged hospitalization, recurrent infection, repeated surgical intervention, and lower-extremity amputation. Their multifactorial development and persistence involve peripheral neuropathy, vascular insufficiency, hyperglycemia, impaired immune defense, and defective tissue regeneration (Dawi et al., 2025). Infection further complicates the clinical course of DFUs and may accelerate tissue destruction, particularly in wounds that fail to respond to conventional antimicrobial and wound-care strategies (Mudrik-Zohar et al., 2022). Identifying severe and non-healing DFUs requires an integrated assessment of wound-associated bacterial communities and the pathophysiology of the affected tissue. Previous studies investigating the DFU microbiome have identified well-known wound pathogens, including *S. aureus*, *Streptococcus* spp., *Enterococcus* spp., *Pseudomonas aeruginosa*, members of the family Enterobacteriaceae, *Acinetobacter baumannii*, and anaerobic genera such as *Prevotella*, *Bacteroides*, *Fusobacterium*, and *Porphyromonas* (Dowd et al., 2008; Huang et al., 2022). Wound healing proceeds through coordinated and regulated interactions among inflammatory cells, fibroblasts, keratinocytes, endothelial cells, and extracellular matrix (ECM) components (Dinh et al., 2012). Altered immune-cell activity and impaired macrophage transition from inflammatory to reparative phenotypes can prolong inflammation within the wound bed (Srivastava et al., 2022). In parallel, excessive matrix metalloproteinase activity contributes to ECM degradation, while dysregulated TGF-β signaling, defective fibroblast activation, and abnormal collagen turnover impair granulation tissue formation and matrix remodeling (Ayuk et al., 2016; Chen et al., 2023). Impaired angiogenesis and vascular dysfunction further restrict oxygen and nutrient delivery to the healing tissue (Piaggesi et al., 2003). Re-epithelialization represents structural wound closure, whereas complete healing also requires restoration of epidermal barrier function (Kundu et al., 2026). Clinically closed chronic wounds may retain impaired barrier function, as demonstrated by elevated post-closure transepidermal water loss. Higher post-closure barrier impairment has been associated with subsequent wound recurrence, indicating that apparent wound closure does not necessarily represent durable functional healing (Chattopadhyay et al., 2024). The chronic wound microenvironment, including reduced oxygen availability, damaged tissue, altered nutrient conditions, antimicrobial exposure, and impaired host defense, may support the persistence of diverse microbial communities (Kalan & Brennan, 2019). Molecular profiling of deep-tissue samples can identify polymicrobial and anaerobic components that may be missed or underrepresented by routine culture (Malone et al., 2017). Biofilm formation within host tissues can increase bacterial tolerance to antimicrobial treatment, thereby contributing to persistent infection and chronic disease (Pouget et al., 2020). Bacterial survival may be further promoted by biofilm-associated mechanisms, as biofilms occur more frequently in chronic than in acute wounds and can increase tolerance to antimicrobial and host-mediated stresses (James et al., 2008). Assessment of biofilm formation and virulence-associated characteristics in representative cultured isolates can therefore provide functional context to sequence-based taxonomic findings. *S. aureus* and *P. aeruginosa* are among the major wound-associated pathogens capable of establishing biofilms in chronic wounds (Neut et al., 2011). Initial attachment to host tissue, bacterial adhesion, and aggregation are followed by the development of structured communities surrounded by an extracellular polymeric substance (EPS) matrix containing polysaccharides, proteins, extracellular DNA, and lipids (Liu et al., 2024). The biofilm matrix and altered physiological states of biofilm-associated cells can reduce susceptibility to antimicrobial agents and host immune clearance, thereby favoring bacterial survival (Lichtenberg et al., 2024). Biofilms may also facilitate horizontal transfer of antimicrobial-resistance genes, providing an

additional mechanism through which resistance determinants can disseminate within bacterial communities (Michaelis & Grohmann, 2023). Persistent wound biofilms are associated with sustained inflammatory responses and can interfere with progression toward effective tissue repair. Nevertheless, although biofilms are associated with chronic wound infection and delayed healing, their contribution within heterogeneous clinical wound environments remains complex and requires further investigation (Lavery et al., 2019). Host gene-expression analysis provides complementary information on the inflammatory and reparative states of DFUs (Theocharidis et al., 2020). IL-8, IFN-γ, IL-2, and MIP-1α/CCL3 were selected to assess immune and inflammatory signaling, which may remain dysregulated in diabetic and other non-healing chronic wounds (Hassan et al., 2025). TGF-β1, α-SMA/ACTA2, MMP-1, FSP-1/S100A4, COL1A1, and COL3A1 were examined to assess fibroblast-associated activity and extracellular matrix remodeling, processes known to be altered in DFU-derived fibroblasts and tissues (Littig et al., 2022; Maione et al., 2016). Disrupted coordination between immune-cell recruitment and tissue repair has also been associated with impaired DFU healing (Sawaya et al., 2020). Evaluating these host responses together with microbial and histopathological findings may therefore provide a more comprehensive biological representation of severe and persistent DFUs. Accordingly, the present study aimed to characterize severe DFUs using an integrated clinical and molecular approach. Clinical and microbiological characteristics were evaluated across the DFU cases, followed by detailed analysis of selected severe, non-healing cases associated with amputation using sequencing of the V3–V4 region of the 16S rRNA gene. Microbial findings were examined in relation to biofilm formation, histopathological changes, and host inflammatory and wound-remodeling gene-expression patterns.

2. Materials and Methods

2.1 Study design and clinical data collection

This prospective observational study was conducted at Mahatma Gandhi Medical College and Research Institute, Puducherry, India, involving 135 patients clinically diagnosed with DFUs. Inclusion criteria comprised patients aged ≥18 years with confirmed diabetes mellitus and DFUs. Exclusion criteria included non-diabetic foot ulcers and incomplete essential clinical records. Demographic, clinical, wound-related, and microbiological data were documented. Among these patients, five undergoing lower-extremity amputation were selected based on clinical severity and the availability of surgically obtained deep-tissue specimens for microbiological, histopathological, and molecular investigations.

2.2. Clinical specimen collection and ethical approval

Deep-tissue specimens were aseptically collected from surgically amputated and debrided diabetic foot tissues. Non-diabetic wound tissue specimens were included as controls for comparative histopathological and gene-expression analyses. Following collection, tissue specimens were divided into separate portions for microbiological, molecular, and histopathological investigations. Samples designated for nucleic acid extraction were immediately preserved in DNA/RNA Shield (Zymo Research, Irvine, CA, USA) for subsequent bacterial 16S rRNA gene sequencing and host gene-expression analysis. Separate tissue portions were collected for bacterial isolation, while specimens intended for histopathological examination were fixed in 10% neutral-buffered formalin. The study protocol was reviewed and approved by the Institutional Human Ethics Committee,

Sri Balaji Vidyapeeth University, Puducherry (MGMCRI/2024/02/IHEC/27). Written informed consent was obtained from the participants in accordance with institutional ethical guidelines and applicable regulations.

2.3. Histopathological examination

Tissue specimens intended for histopathological examination were fixed in 10% formalin. Amputated DFU and non-diabetic wound tissue specimens designated for histopathology were fixed in 10% formalin, subjected to routine tissue processing, and embedded in paraffin. Sections of 5µm were prepared and stained with hematoxylin and eosin (H&E). Histological examination was performed using light microscopy to evaluate epidermal, dermal, and subcutaneous tissue alterations.

2.4. DNA extraction and 16S rRNA V3–V4 amplicon sequencing

Genomic DNA was extracted from five amputated DFU deep-tissue specimens for bacterial 16S rRNA gene amplicon sequencing. DNA concentration, sample volume, and V3–V4 amplicon quality-control results are presented in Supplementary Table S4. The V3–V4 hypervariable region of the bacterial 16S rRNA gene was amplified, and the resulting amplicon libraries were sequenced using the Illumina NextSeq 2000 platform (Illumina, San Diego, CA, USA); raw sequencing data were processed using QIIME 2 (Bolyen et al., 2019), including sequence-quality assessment and preprocessing. Chimeric sequences were identified and removed using VSEARCH (Rognes et al., 2016). Quality-filtered sequences were clustered into operational taxonomic units (OTUs) at 97% sequence similarity using VSEARCH (Rognes et al., 2016). Taxonomic classification was performed against the SILVA 138 reference database (Quast et al., 2013). The resulting OTU abundance table and taxonomic assignments were used to characterize bacterial community composition across the five deep-tissue specimens.

2.5. Bacterial isolation and identification

Aseptically collected amputated DFU deep-tissue specimens were processed for aerobic and anaerobic bacterial isolation using conventional culture-based methods. For aerobic bacterial isolation, tissue specimens were inoculated into Luria–Bertani (LB) broth (HiMedia Laboratories, Mumbai, India), followed by cultivation on LB agar under aerobic conditions. For anaerobic bacterial isolation, tissue specimens were enriched in Todd–Hewitt broth (HiMedia) and subsequently inoculated onto Todd–Hewitt agar supplemented with hemin (5 µg/mL) and vitamin K_1 (5 µg/mL). Anaerobic cultures were incubated in an atmosphere containing 80% N_2, 10% H_2, and 10% CO_2. Recovered bacterial isolates were subjected to identification and further characterization.

2.6. Biofilm cultivation and time-dependent assessment

Bacterial isolates recovered from amputated DFU tissues were used for biofilm cultivation. Aerobic isolates were cultured in Luria–Bertani (LB) broth (HiMedia Laboratories, Mumbai, India) at 37 °C under aerobic conditions, and biofilm development was assessed at 6, 24, and 48 h. Anaerobic isolates were cultured in Todd–Hewitt broth (HiMedia) supplemented with hemin (5 µg/mL) and vitamin K_1 (5 µg/mL) at 37 °C under anaerobic conditions for 3–5 days. Biofilms were established on sterile glass slides placed in Petri dishes and incubated anaerobically at 37 °C for 24, 48, and 72 h. The experimental approach to biofilm cultivation and characterization was informed by previous biofilm investigations (Gopalakrishnan et al., 2025; Gopalakrishnan et al., 2024). Biofilm biomass was assessed using crystal violet staining (O'Toole, 2011), while extracellular matrix-associated proteins were

visualized using FilmTracer SYPRO Ruby Biofilm Matrix Stain according to the manufacturer's protocol (Thermo Fisher Scientific). Biofilm morphology and structural organization were examined using scanning electron microscopy (SEM), following established imaging procedures (Fischer et al., 2024).

2.7. Crystal violet staining and fluorescence microscopy

Biofilm formation on glass slides was examined using crystal violet and fluorescence staining. Adherent bacterial biomass was stained with 0.1% crystal violet (200 µL) for 30 min, followed by gentle rinsing with distilled water to remove residual dye. Biofilm attachment and structural organization were subsequently examined by light microscopy. For fluorescence-based visualization of matrix-associated proteins, biofilm-coated slides were incubated with 200 µL of FilmTracer™ SYPRO® Ruby Biofilm Matrix Stain (Thermo Fisher Scientific, Waltham, MA, USA) for 30 min. Following removal of excess stain by gentle washing, the slides were examined under a fluorescence microscope to assess the distribution and organization of the proteinaceous biofilm matrix.

2.8. RNA Extraction and Gene Expression Profiling

Total RNA was extracted from DFU and non-diabetic wound tissue specimens preserved in DNA/RNA Shield using the TRIzol reagent method. Complementary DNA (cDNA) was synthesized from 1 µg of total RNA using the PrimeScript RT-PCR Kit (Takara) according to the manufacturer's instructions. Quantitative real-time PCR (RT-qPCR) was performed using SYBR Premix Ex Taq™ (Takara) to evaluate the expression of genes associated with inflammation, immune regulation, fibroblast activation, extracellular matrix remodeling, and collagen synthesis. The selected gene panel comprised inflammatory and immune-associated genes, including IL8 (interleukin-8; IL-8), IL2 (interleukin-2; IL-2), IFNG (interferon-γ; IFN-γ), and CCL3 (C-C motif chemokine ligand 3; macrophage inflammatory protein-1α, MIP-1α); fibroblast- and myofibroblast-associated genes, including S100A4 (S100 calcium-binding protein A4; fibroblast-specific protein-1, FSP-1), VIM (vimentin), ACTA2 (α-smooth muscle actin, α-SMA), and TGFB1 (transforming growth factor-β1; TGF-β1); the extracellular matrix-remodeling gene MMP1 (matrix metalloproteinase-1; MMP-1); and collagen-associated genes COL1A1 (collagen type I α1 chain) and COL3A1 (collagen type III α1 chain). The forward and reverse primer sequences, corresponding gene targets, and annealing temperatures used for RT-qPCR analysis are provided in Table S6. RT-qPCR reactions were performed in PCR strips with a total reaction volume of 10 µL, comprising 1 µL of cDNA, 5 µL of SYBR Green Master Mix, 0.2 µL of each primer (100 µM stock concentration), and 3.6 µL of RNase-free water. Thermal cycling conditions consisted of an initial denaturation at 95 °C for 3 min, followed by 40 cycles of denaturation at 95 °C for 5 s, annealing at 60 °C for 30 s, and extension at 72 °C for 20 s. Quantification cycle (Cq) values were determined using the instrument software with default analysis settings. All RT-qPCR measurements were performed in triplicate. Target gene expression was normalized to ACTB (β-actin), which served as the reference gene. Relative gene expression in DFU tissues compared with non-diabetic wound tissues was calculated using the $2^{-}\Delta\Delta Cq$ method. Statistical analyses were performed using GraphPad Prism software. Differences in gene expression between the groups were evaluated using appropriate parametric or non-parametric statistical tests, with $p < 0.05$ considered statistically significant.

2.9. Statistical and bioinformatic analysis

Processed 16S rRNA sequencing data from five amputated DFU specimens were analyzed to characterize microbial diversity and taxonomic composition. Alpha diversity was assessed using rarefaction analysis, Chao1

richness, Shannon diversity, and the inverse Simpson index. Beta diversity was evaluated using Bray–Curtis dissimilarity and principal coordinate analysis (PCoA). Downstream bioinformatic analyses and visualizations were performed using R statistical software (version 4.6.1; R Foundation for Statistical Computing, Vienna, Austria; https://www.r-project.org/). Taxonomic abundance data were processed using the dplyr and tidyr packages, while ggplot2, scales, and patchwork were used to generate relative abundance plots, heatmaps, and taxonomic distribution profiles. Shared and sample-specific bacterial taxa were visualized using the VennDiagram package. Statistical analyses of host gene expression were performed using GraphPad Prism software. Relative gene expression was calculated using the comparative 2^−ΔΔCt method. Differences between DFU and non-diabetic wound tissues were evaluated using a two-tailed unpaired Student's t-test. Data were expressed as mean ± standard error of the mean (SEM). A p-value < 0.05 was considered statistically significant.

3. Results

Clinical information was evaluated for 135 subjects with DFUs, including demographic characteristics, diabetes duration, wound manifestations, and associated comorbidities (Table S1). Five severe DFU cases undergoing lower-limb amputation were selected for detailed deep-tissue investigations. Representative pre-amputation clinical photographs illustrating the wound characteristics of these five cases are presented in Figure 1A–E. Their clinical characteristics, conventional culture findings, antimicrobial susceptibility profiles, and selected biochemical parameters are summarized in Table S2.

3.1 Severe DFU tissues displayed marked inter-sample differences in bacterial diversity.

Sequencing quality metrics indicated consistently high base-call quality across all five DFU tissue specimens, with mean Phred scores ranging from 30.30 to 32.73 for forward reads (R1) and 30.09 to 32.30 for reverse reads (R2). The proportion of bases exceeding Q30 ranged from 78.68% to 92.62% for R1 and 77.12% to 90.13% for R2 (Table S3). Rarefaction curves reached near-stable levels, indicating that the sequencing depth was sufficient to capture the bacterial diversity in the samples (Fig. 2A). The inverse Simpson diversity index, which reflects both the number of taxa and their relative distribution within the community, ranged from approximately 1.0–3.6 (Fig.2B). Chao1 richness estimates ranged from 67.75 to 272.00, while Shannon diversity indices ranged from 0.48 to 4.39, demonstrating variation in bacterial richness and community diversity among the five DFU tissue specimens (Fig. 2C; Table S4). Beta-diversity analysis using Bray–Curtis principal coordinate analysis (PCoA) was used to compare the bacterial community composition between the tissue samples (Fig. 2D). The first and second axes explained 38.2% and 28.0% of the variation, respectively, accounting for 66.2% of the total variation (Fig. 3). Venn analysis demonstrated substantial heterogeneity in the bacterial composition of the five amputated DFU tissue types (Fig. 4). A total of 29 genera were uniquely detected in the individual tissues. Among these sample-specific genera, 20 accounted for 69.0%, six for 20.7%, two for 6.9%, and one for 3.4% of the total abundance. Two genera were consistently shared across all five tissues, indicating that only a small core microbiome was present in DFU tissues. Several additional genera were shared between two or more tissues, indicating a partial taxonomic overlap. The predominance of unique genera and the limited number of universally shared genera indicate a highly diverse and heterogeneous polymicrobial community in amputated DFUs.

3.2 Distinct microbial configurations characterize the deep-tissue DFU microbiome.

At the phylum level, the bacterial profiles were dominated by Proteobacteria, Actinobacteriota, Firmicutes, and Bacteroidota (Fig. 5A). Proteobacteria accounted for 99.7% and 99.8% of the 99.8% reads in the two profiles. In contrast, Actinobacteriota represented 62.3% and 96.0% of the reads in the profiles. The remaining profile was characterized predominantly by Bacteroidota (49.5%), together with a high proportion of Firmicutes (Fig. 5B). Lower-abundance groups included Lachnospiraceae, Staphylococcaceae, and members of Peptostreptococcales–Tissierellales (Fig. 5C). Genus-level analysis further revealed differences in microbial composition between tissues (Fig. 6A). *Corynebacterium* and *Acinetobacter* showed the highest cumulative abundance across the dataset (Fig. 6B). Other represented genera included *Porphyromonas, Escherichia–Shigella, Veillonella, Parvimonas, Staphylococcus, Prevotella, Atopobium, Paracoccus*, and *Brevibacterium*. The dominant genera showed differences between individual tissues (Fig. 6C). The heatmap of the 50 most abundant genera demonstrated distinct sample-specific abundance patterns (Fig. 7). Several bacterial genera were strongly represented in individual tissues, whereas others were distributed across multiple samples at lower or intermediate relative abundances.

3.3 Dominant bacterial taxa and their enrichment patterns in amputated DFU tissues

The distribution of dominant bacterial taxa demonstrated a heterogeneous and polymicrobial community across amputated DFU tissues (Fig. 8A). The relative-abundance patterns varied considerably across the tissues; *Corynebacterium* and *Acinetobacter* showed the highest overall abundance, while *Escherichia–Shigella, Porphyromonas, Veillonella, Streptococcus,* and *Staphylococcus* contributed substantially to the microbial profiles (Fig. 8B). Other genera, including *Parvimonas, Prevotella, Fusobacterium,* and *Solobacterium*, were also detected, indicating the coexistence of aerobic, facultative, and anaerobic bacteria (Fig. 8C). Enrichment analysis further demonstrated differences in the distribution of the dominant taxa (Fig. 9A). Along with *Corynebacterium* and *Acinetobacter*, anaerobic or anaerobe-associated genera, particularly *Porphyromonas, Veillonella, Parvimonas, Fusobacterium,* and *Solobacterium*, showed variable enrichment across the tissues (Fig. 9B). Overall, these findings demonstrate that severe DFU tissues contain mixed bacterial communities characterized by prominent opportunistic taxa and an increased anaerobic culture (Fig. 9C).

3.4 Histopathological features of chronic Amputated DFU tissues

Histopathological examination showed marked alterations in epidermal, dermal, and subcutaneous tissue architecture in amputated DFU specimens. Epidermal hyperplasia, hyperkeratosis, acanthosis, and focal disruption of the epidermal architecture were observed (Fig.10A). The underlying dermis showed prominent fibrocollagenous tissue with altered collagen organization and stromal remodeling (Fig. 10B). Dense inflammatory-cell infiltration involving the dermal compartment, with disruption of the surrounding tissue architecture, was evident in severely affected areas (Fig. 10C). Non-diabetic chronic wound tissues also showed inflammatory and reparative histological changes. Epidermal and dermal alterations were accompanied by inflammatory-cell infiltration and fibrocollagenous stromal changes (Fig. 10D). In some sections, inflammatory infiltration extended into the deeper tissue and subcutaneous adipose compartment (Fig. 10E). Other areas showed fibrocollagenous remodeling with focal inflammatory-cell infiltration within the deeper wound tissue (Fig. 10F).

Additional findings identified across the examined amputated DFU specimens included focal ulceration, dermal edema, abscess formation, panniculitis, tissue necrosis, fibrocollagenous destruction, vascular congestion and dilatation, fibrin thrombi, vessel-wall thickening, luminal narrowing, perineural edema, and bacterial colonies. These histopathological findings indicate extensive involvement of epidermal, connective-tissue, inflammatory, vascular, and neurovascular compartments in severe amputated DFUs.

3.5 Taxonomically distinct Amputated DFU isolates showed progressive biofilm formation.

Biofilm formation was evaluated in three representative bacterial isolates recovered from amputated DFU tissues, *A. baumannii*, *S. aureus*, and *Solobacterium* sp., representing distinct taxonomic and physiological groups. *A. baumannii* and *S. aureus* were evaluated at 6, 24, and 48 h, whereas *Solobacterium* sp. was evaluated over an extended anaerobic incubation period at days 2, 4, 8, and 16. In *A. baumannii*, crystal violet staining showed initial surface attachment at 6 h (Fig. 11A), followed by increased cellular aggregation and microcolony formation at 24 h (Fig. 11B) and greater surface-associated biomass at 48 h (Fig. 11C). SYPRO® Ruby staining showed discrete matrix-associated fluorescence at 6 h (Fig. 12A), increased fluorescence associated with bacterial aggregates at 24 h (Fig. 12B), and extensive matrix-associated fluorescence at 48 h (Fig. 12C). *S. aureus* showed a similar temporal pattern, with initial bacterial attachment at 6 h (Fig. 13A), increased cellular aggregation and microcolony formation at 24 h (Fig. 13B), and greater adherent biomass at 48 h (Fig. 13C). Correspondingly, SYPRO® Ruby staining showed initial matrix-associated fluorescence at 6 h (Fig. 14A), increased fluorescence associated with bacterial aggregates at 24 h (Fig. 14B), and extensive matrix-associated fluorescence at 48 h (Fig. 14C). *Solobacterium* sp. exhibited biofilm-associated development over a prolonged anaerobic incubation period. Crystal violet staining showed dispersed surface-associated growth with localized bacterial aggregation at day 2 (Fig. 15A), more prominent cellular aggregation and adherent growth at day 4 (Fig. 15B), extensive surface-associated growth with larger and more widely distributed bacterial aggregates at day 8 (Fig. 15C), and dense adherent bacterial organization with extensive surface-associated biomass at day 16 (Fig. 15D). SYPRO® Ruby staining showed scattered matrix-associated fluorescence at day 2 (Fig. 16A), increased and more widely distributed fluorescence at day 4 (Fig. 16B), extensive matrix-associated fluorescence at day 8 (Fig. 16C), and dense, broadly distributed matrix-associated fluorescence at day 16 (Fig. 16D), consistent with an EPS-rich biofilm matrix. These observations demonstrate prolonged, day-scale development of an adherent, matrix-associated biofilm phenotype by *Solobacterium* sp. under anaerobic culture conditions.

3.6 Amputated DFU Tissues Exhibit Altered Inflammatory and Extracellular Matrix Remodeling Gene Expression

Quantitative gene-expression analysis demonstrated alterations in inflammatory, fibroblast-associated, matrix-remodeling, and extracellular matrix (ECM) related markers between DFU and control tissues. α-Smooth muscle actin (α-SMA/ACTA2) expression was significantly increased in DFU tissues compared with controls ($p < 0.05$), with some specimens showing more than two-fold expression (Fig. 16A). MMP-1 expression was markedly increased, reaching a mean of approximately six-fold relative to controls ($p < 0.0001$), with several DFU specimens exhibiting expression above ten-fold (Fig. 16B). IFN-γ expression showed no significant difference between DFU and control tissues (Fig. 16C). IL-8 expression was markedly increased in DFU tissues, with a mean expression of approximately five-fold and individual specimens reaching approximately 15-fold ($p < 0.0001$) (Fig. 16D). IL-2 was also significantly increased, with expression centered at approximately two-fold relative to

controls ($p < 0.0001$) (Fig. 16E). TGF-β expression was significantly increased in DFU tissues ($p < 0.01$), with several specimens exhibiting pronounced increases (Fig. 16F). FSP-1/S100A4 expression was significantly increased in DFU tissues compared with controls ($p < 0.05$) (Fig. 16G). COL-I/COL1A1 expression was significantly reduced in DFU tissues ($p < 0.05$) (Fig. 16H). In contrast, COL-III/COL3A1 expression was significantly increased, with a mean expression of approximately three-fold ($p < 0.0001$), and several specimens showing substantially higher expression (Fig. 16I). Vimentin (VIM) expression was markedly increased in DFU tissues ($p < 0.0001$) (Fig. 16J). MIP-1 expression was also significantly increased in DFU tissues compared with controls ($p < 0.001$) (Fig. 16K). Overall, the amputated DFU tissues exhibited concurrent inflammatory activation, increased matrix-remodeling activity, altered fibroblast-associated marker expression, and differential regulation of type I and type III collagen genes.

4. Discussion

Persistent biofilms within chronic wound tissue can alter host–microbial interactions, sustain inflammatory responses, and interfere with cellular and matrix-remodeling processes required for effective wound healing (Kalan & Brennan, 2019; Loesche et al., 2017). Severe DFUs may therefore enter a self-perpetuating state in which tissue damage provides conditions that favor microbial persistence. However, persistent microbial communities can further interfere with resolution of inflammation and tissue repair (Johani et al., 2017). Within our prospective DFU cohort, five severe cases that progressed to amputation were selected for detailed investigation to characterize the microbial and tissue alterations associated with advanced wound severity and adverse clinical outcomes. Diabetic foot infections harbor complex polymicrobial communities, with molecular sequencing approaches detecting a broader diversity of anaerobic taxa than conventional culture (Kalan et al., 2019; Villa et al., 2024). Similarly, 16S rRNA sequencing identified an average of 66.1 bacterial genera compared with 1.5 by routine culture. Anaerobic bacteria accounted for 59% and 76% of metagenomic sequencing, respectively, compared with 26% by conventional culture. Further analysis revealed heterogeneous polymicrobial communities comprising *Acinetobacter, Staphylococcus, Streptococcus, Corynebacterium, and Escherichia–Shigella*, together with anaerobic taxa including *Prevotella, Porphyromonas, Veillonella, Parvimonas, Fusobacterium, and Solobacterium*. Strict anaerobes were especially frequently identified in myiasis-associated wounds that progressed to amputation, including *Fusobacterium* and *S. moorei*. The presence of abscesses and deeper inflammatory involvement indicates that the inflammatory response extends beyond the ulcerated surface, whereas necrosis and matrix destruction reflect substantial loss of tissue integrity. Voza et al. (2024) reported that poor outcomes in surgically treated DFUs were associated with increased neutrophil accumulation and reduced fibroblast and endothelial cell distribution in the wound bed. In addition to inflammatory and structural tissue damage, amputated DFU tissues showed vessel-wall thickening, luminal narrowing, vascular congestion, and fibrin thrombi, indicating marked microvascular injury. Such vascular abnormalities may impair local tissue perfusion and oxygen delivery, thereby creating conditions that could favor the persistence of anaerobic bacteria. Tissue disruption may also provide surfaces permissive to bacterial attachment and the establishment of persistent microbial communities. The gene expression findings showed that host inflammatory and tissue remodeling responses remained active despite severe tissue damage. Increased IL-8 (CXCL8) expression, together with dense inflammatory-cell infiltration, enhances persistent inflammatory activity within the DFU tissue. Rai et al. (2022) reported CXCL8/IL-8 as an important mediator of persistent inflammation and altered fibroblast responses in non-healing DFUs, consistent with increased IL-8 expression. Increased *MMP1* expression and ECM disruption

support continued extracellular matrix turnover within the damaged tissue. In chronic DFU tissue, increased *MMP1* expression was observed in the presence of persistent inflammation, suggesting that active-matrix remodeling did not result in restoration of normal tissue architecture. The altered collagen profile further supports incomplete matrix maturation. Increased COL3A1 expression, together with downregulated COL1A1 expression, may reflect continued formation and remodeling of an early collagen matrix without progression toward a mature type I collagen-rich matrix. In parallel, increased expression of transforming growth factor-beta (TGF-β), alpha-smooth muscle actin (α-SMA/ACTA2), fibroblast-specific protein-1 (FSP1/S100A4), and vimentin indicated that fibroblast/myofibroblast-associated responses were retained in severely amputated DFU tissues. TGF-β is an important regulator of fibroblast activation, myofibroblast differentiation, ECM synthesis, and collagen deposition through the TGF-β/SMAD signaling axis. The presence of these fibroblast/myofibroblast-associated markers, together with altered collagen expression and fibrocollagenous destruction, suggests that the reparative response remained active but was insufficient to restore normal matrix organization. Inflammatory signaling, fibroblast/myofibroblast activity, and ECM remodeling remained concurrently upregulated in severe DFU tissue. Chen and Zou. (2024) reported differences in fibroblast populations and ECM-related signaling between healing and non-healing DFUs. The combined increase in inflammatory and fibroblast-associated markers, altered collagen expression, and histological tissue damage caused a failure of the normal transition from inflammation to matrix maturation, resulting in continued tissue remodeling without stable structural repair. Thus, the histological evidence of fibrocollagenous disruption and molecular evidence of continued matrix activity suggest that matrix synthesis and remodeling were occurring without effective tissue reconstruction. Persistent biofilm-associated microbial communities may deliver a continuing source of microbial stimuli within the damaged tissue environment, potentially contributing to prolonged inflammatory and remodeling activity. Conversely, incomplete tissue restoration may maintain exposed and structurally altered tissue surfaces that remain favorable for microbial attachment and persistence. Impaired chronic DFU healing may not reflect the absence of inflammatory or reparative activity but rather a failure to progress from persistent activation toward resolution and restoration. The wound remains inflamed, the extracellular matrix continues to be remodeled, and fibroblast-associated pathways remain active. However, re-epithelialization, collagen maturation, and restoration of organized tissue architecture remain incomplete. *A. baumannii* and *S. aureus* showed progressive biofilm formation. A notable finding was the detection of the strict anaerobe *S. moorei* in deep amputated DFU tissue, which exhibited biofilm-associated growth over several days under anaerobic conditions. This finding is biologically relevant because chronic, deep DFUs can develop oxygen-limited and necrotic microenvironments that favor strict anaerobes (Zheng et al., 2010). Increased hypoxic conditions are recognized as an important feature of impaired diabetic wound healing (Dinh et al., 2012). Thus, the deep-tissue occurrence and biofilm-forming phenotype of *S. moorei* suggest that oxygen-limited niches in severe DFUs may support the persistence of slow-growing anaerobic communities that can be underestimated by conventional culture. In contrast, the DFU tissues showed inflammatory cell infiltration and increased IL-8 expression. Persistent tissue damage observed in severe DFUs may provide conditions that favor bacterial attachment and biofilm formation, increase the expression of the inflammatory environment, and result in delays in effective tissue restoration. Established, biofilm-associated bacterial communities may remain within the wound and maintain prolonged interactions with the surrounding host tissue. The hypoxic and poorly perfused microenvironment of chronic DFUs may establish oxygen-limited ecological niches that facilitate the persistence of obligate anaerobes within deeper tissues. Anaerobic bacteria are increasingly recognized as

components of polymicrobial DFU communities and biofilms (Alauzet et al., 2021). So, they act as a microbial reservoir within severe DFUs, potentially contributing to persistent host–microbial interactions and sustained inflammatory activity. Such persistent microbial activity may contribute to continued inflammatory and matrix-remodeling responses, preventing the wound from progressing toward effective re-epithelialization, collagen maturation, and restoration of tissue architecture. Thus, biofilm-associated persistence and impaired tissue repair may represent interconnected processes that reinforce one another during chronic wound progression.

5. Conclusion

This study provides an integrated view of amputated DFUs characterized by heterogeneous bacterial communities, extensive tissue damage, biofilm-forming bacterial isolates, and altered host repair responses. Deep-tissue 16S rRNA profiling revealed *Acinetobacter*-dominant, *Corynebacterium*-rich, and anaerobe-enriched communities, including *Porphyromonas, Veillonella*, and *Solobacterium*. The presence of *Solobacterium* in amputated DFU tissue highlights the emergence of microbial complexity in severe DFUs. To our knowledge, this study is the first to report the prevalence of *S. moorei biofilm* in deep tissue from a DFU requiring amputation. The detection of diverse anaerobic taxa in deep tissues further expanded the microbial profile of severe amputated DFUs beyond organisms commonly identified by conventional culture. Together, these findings demonstrate the coexistence of heterogeneous bacterial communities, severe tissue injury, biofilm-forming phenotypes, and altered host repair responses in severe DFUs.

Figures

Fig. 1. Clinical manifestations of severe diabetic foot ulcers requiring amputation. **A)** Diabetic great-toe ulcer with deep soft-tissue involvement. **(B)** Extensive diabetic foot ulcer with widespread ulceration and tissue destruction. **(C)** Deep ulcerative lesion involving the ankle region with exposed underlying tissue. **(D)** Diabetic great-toe ulcer with extensive tissue necrosis. **(E)** Diabetic forefoot ulcer with gangrenous tissue changes.

Fig. 2. Bacterial diversity across individual DFU tissue samples. A. Rarefaction curves showing the accumulation of observed operational taxonomic units (OTUs) with increasing sequencing depth across DF-01–DF-05. The approach towards a plateau indicates the extent of sequencing coverage for the bacterial communities detected in each sample. **B.** Alpha diversity assessed using the Inverse Simpson index, which incorporates both taxonomic richness and evenness; values for individual DFU tissue samples are indicated above each point. **C.** Chao1 richness estimates for DF-01–DF-05, representing estimated bacterial taxonomic richness within each sample; numerical values are indicated adjacent to each point. **D.** Principal coordinate analysis (PCoA) based on Bray–Curtis dissimilarity showing differences in bacterial community composition among individual DFU tissue samples. Each point represents one DFU tissue sample, and PCoA1 and PCoA2 account for 53.85% and 29.16% of the total variation, respectively

Fig. 3. Community configuration of individual DFU tissue samples based on Bray–Curtis dissimilarity. Principal coordinate analysis (PCoA) based on Bray–Curtis dissimilarity showing variation in bacterial community composition among DF-01–DF-05. Each point represents an individual DFU tissue sample, with triangles indicating samples provisionally classified as aerobe/skin-dominant (DF-01, DF-03 and DF-04) and circles indicating enteric/anaerobe-rich samples (DF-02 and DF-05) based on their taxonomic composition.

PCoA1 and PCoA2 account for 26.3% and 25.3% of the variation in community composition, respectively. Connecting lines delineate the samples assigned to each provisional microbial profile.

Fig. 4. Shared and sample-specific bacterial taxa across individual DFU tissue samples. Five-set Venn diagram showing the distribution and overlap of bacterial taxa detected by 16S rRNA sequencing across DF-01–DF-05. Each colored ellipse represents the bacterial taxa detected within an individual DFU tissue sample. Numbers within non-overlapping regions indicate taxa detected exclusively in the corresponding sample, whereas numbers within intersecting regions indicate taxa shared between the respective samples. The central intersection represents bacterial taxa detected across all five DFU tissue samples.

Fig. 5. Taxonomic composition of bacterial communities across individual DFU tissue samples. **A.** Phylum-level relative abundance profiles across DF-01–DF-05. Stacked bars represent the proportion of sequencing reads assigned to each major bacterial phylum within individual samples, expressed as relative abundance (%); low-abundance taxa and sequences without phylum-level taxonomic assignment are grouped as "Other" and "Unassigned," respectively. **B.** Dominant bacterial phylum identified in each DFU tissue sample. Horizontal bars indicate the relative abundance (%) of the most abundant phylum in each sample, with the corresponding taxonomic assignment and abundance indicated adjacent to each bar. **C.** Family-level taxonomic profiles showing the relative abundance of the ten major bacterial families across DF-01–DF-05. Stacked bars represent the proportional contribution of each family to the bacterial community within each sample, with families outside the displayed taxa collectively represented as "Other."

Fig. 6. Genus-level bacterial composition across individual amputated DFU tissue samples. A. Genus-level relative abundance profiles of bacterial communities across DF-01–DF-05. Stacked bars represent the proportional abundance of the major bacterial genera within each sample, expressed as percentage relative abundance; genera outside the individually displayed taxa are grouped as "Other." **B.** Major bacterial genera ranked according to their summed relative abundance across the five DFU tissue specimens (DF_01–DF_05). Horizontal bars represent the summed relative abundance (%) of each genus across DF-01–DF-05. **C.** Distribution of the dominant bacterial genus within each individual DFU tissue sample. The position of each point represents the relative abundance (%) of the predominant genus, while point size is proportional to its relative abundance; genus labels indicate the predominant taxon identified in each sample.

Fig. 7. Hierarchical clustering and abundance patterns of bacterial taxa across individual DFU tissue samples. Heatmap showing row-wise standardized relative abundance profiles of selected bacterial taxonomic assignments across DF_01–DF_05. Rows represent bacterial taxa identified from 16S rRNA sequencing, and columns represent individual DFU tissue samples. Values are presented as row-wise Z-scores of relative abundances, with warmer colors indicating higher and cooler colors indicating lower abundance relative to the mean abundance of each taxon across samples. Hierarchical clustering of taxa and samples was performed using Euclidean distance and complete linkage, as represented by the corresponding dendrograms.

Fig. 8. Distribution of dominant bacterial taxa across individual amputated DFU tissue samples. **a.** Circular taxonomic representation of bacterial taxa detected by 16S rRNA sequencing in DFU tissue samples, illustrating the distribution of selected genera and species-level assignments within the bacterial community. Nodes represent bacterial taxa and connecting branches indicate their taxonomic organization. **b.** Relative abundance profiles of dominant bacterial taxa across individual DFU tissue samples (DF-01–DF-05). Stacked bars represent the proportion of sequencing reads assigned to each displayed taxon within each sample, expressed as relative abundance (%); taxa outside the individually displayed categories are grouped as "Other taxa". **c.** Descriptive comparison of the mean relative abundance of selected bacterial taxa between the provisionally classified aerobe/skin-dominant (DF_01, DF_03, and DF_04) and enteric/anaerobe-rich (DF_02 and DF_05) microbial profiles.

Fig. 9. Abundance and sample-level distribution of major bacterial taxa in amputated DFU tissues. **A.** Absolute sequence abundance of ten selected bacterial genera identified through 16S rRNA sequencing across five individual DFU tissue samples (DF-01–DF-05). Horizontal bars represent the total number of sequencing reads assigned to each genus, pooled across the five samples and arranged in descending order of abundance. **B.** Log-transformed sequence abundance of the corresponding bacterial genera. Read counts were transformed using $\log_{10}$ (reads + 1) to accommodate differences in sequencing abundance and facilitate visualization of both highly abundant and less abundant taxa. **C.** Sample-level distribution of selected bacterial genera across DF-01–DF-05. The bubble plot represents genus-specific sequencing read abundance within individual DFU tissue samples, with bubble size proportional to the number of reads assigned to each genus. Colors distinguish the bacterial genera, allowing visualization of their distribution and abundance patterns across individual samples.

Fig. 10. Histopathological features of amputated DFU and non-diabetic chronic wound tissues. Representative hematoxylin and eosin (H&E)-stained tissue sections illustrating epidermal and dermal alterations in diabetic foot ulcers (DFUs; A–C) and non-diabetic chronic wounds (D–F). **A.** DFU tissue showing marked epidermal thickening with acanthosis, hyperkeratosis, and elongation of rete ridges, accompanied by disruption of the superficial epidermal architecture. **B.** DFU tissue displaying prominent fibrocollagenous deposition and altered dermal architecture beneath the epidermis. **C.** DFU tissue showing inflammatory cell infiltration within the dermal connective tissue, with associated disruption of normal tissue organization. **D**. Non diabetic chronic wound tissue exhibiting epidermal thickening and inflammatory cell infiltration within the superficial dermis. **E.** Non diabetic chronic wound tissue showing dense inflammatory infiltrates extending into deeper connective tissue and adjacent adipose tissue. **F.** Non diabetic chronic wound tissue demonstrating inflammatory cell accumulation and fibrocollagenous tissue remodeling within the dermis

Fig. 11. ***A. baumannii* biofilm formation assessed by crystal violet staining.** Representative light microscopy images showing the development of surface-associated biofilms by *A. baumannii* at different incubation periods. **A.** Initial bacterial attachment and formation of dispersed cellular aggregates after 6 h of incubation. **B.** Increased surface colonization and development of bacterial aggregates after 12 h. **C.** Formation of more extensive, densely

packed bacterial microcolonies with increased crystal violet staining after 24 h. **D.** Extensive surface-associated bacterial aggregation and dense crystal violet-stained biomass after 48 h of incubation.

Fig. 12. *A. baumannii* biofilm matrix assessed by SYPRO® Ruby staining. Representative fluorescence microscopy images showing the distribution and organization of the biofilm matrix formed by *A. baumannii* at different incubation periods. **A.** At 6 h, dispersed fluorescent signals indicate the presence of surface-associated bacterial aggregates and stained matrix material. **B.** At 12 h, fluorescence appears more interconnected, with localized regions of increased matrix-associated staining. **C.** At 24 h, extensive fluorescent regions and densely distributed signals are observed, indicating greater surface coverage by stained biofilm material. **D.** At 48 h, widespread fluorescence is visible across the microscopic field, consistent with extensive surface-associated biofilm matrix organization. FilmTracer™ SYPRO® Ruby biofilm matrix stain was used to visualize protein-associated components of the extracellular biofilm matrix.

Fig. 13. *S. aureus* biofilm formation assessed by crystal violet staining. Representative light micrographs illustrating the morphological organization of surface-associated *S. aureus* biofilms at successive incubation intervals. **A.** At 6 h, adherent bacterial aggregates exhibit a heterogeneous distribution with discontinuous surface coverage. **B.** At 12 h, larger and more interconnected bacterial clusters are observed, with irregular unstained regions between aggregates. **C.** At 24 h, extensive crystal violet-positive areas are evident, comprising densely aggregated bacterial biomass interspersed with regions of lower staining intensity. **D.** At 48 h, the biofilm exhibits widespread surface coverage with a heterogeneous arrangement of densely stained bacterial assemblies. Collectively, the micrographs illustrate temporal changes in the spatial distribution and organization of adherent bacterial biomass over 48 h.

Fig. 14. ***S. aureus* biofilm matrix assessed by SYPRO® Ruby staining.** Representative fluorescence micrographs of *S. aureus* biofilms stained with FilmTracer™ SYPRO® Ruby biofilm matrix stain at 6, 12, 24, and 48 h of incubation. **A.** At 6 h, fine, punctate fluorescent signals are distributed across the field, with localized regions of increased staining. **B.** At 12 h, closely associated fluorescent structures form more extensive regions of surface coverage, interspersed with areas of reduced fluorescence. **C.** At 24 h, the staining pattern becomes more diffuse and spatially continuous, with broad fluorescent regions and scattered unstained areas. **D.** At 48 h, widespread fluorescence is observed, with localized regions of concentrated signal within a comparatively uniform fluorescent background.

Fig. 15. ***S. moorei* biofilm formation assessed by crystal violet staining.** Representative light micrographs showing crystal violet-stained, surface-associated *S. moorei* biomass following 2, 4, 8, and 16 days of anaerobic incubation. **A.** Day 2, scattered bacterial aggregates and dispersed crystal violet-positive deposits are observed across the surface. **B.** Day 4, localized clusters of densely stained bacteria become more apparent, interspersed with areas of dispersed adherent biomass. **C.** Day 8, larger and more numerous bacterial aggregates are distributed across the field, exhibiting heterogeneous staining patterns and irregular spatial organization. **D.** Day 16: extensive

crystal violet-positive aggregates occupy substantial regions of the surface, with areas of closely associated bacterial biomass.

Fig. 16. ***S. moorei*** **biofilm matrix assessed by SYPRO® Ruby staining.** Representative fluorescence micrographs illustrating the spatial distribution of protein-associated biofilm material following 2, 4, 8, and 16 days of anaerobic incubation. **A.** Day 2: dispersed punctate fluorescence and irregularly distributed fluorescent aggregates are visible, with substantial regions lacking detectable signal. **B.** Day 4: fluorescence extends across larger areas of the field, displaying a heterogeneous distribution of closely associated fluorescent structures. **C.** Day 8: broad regions of fluorescence are interspersed with irregular, non-fluorescent spaces, indicating spatial heterogeneity in the distribution of stained biofilm material. **D.** Day 16: extensive fluorescent structures form a comparatively continuous, irregularly organized network across the field.

Fig. 17. **Gene-expression profile in amputated DFU and non-DFU chronic wound tissues.** Relative gene expression profiles of inflammatory, fibroblast-associated, and extracellular matrix-remodeling markers in diabetic foot ulcer (DFU) tissues and non-diabetic wound controls, assessed by quantitative reverse-transcription PCR (RT-qPCR). **(A)** α-Smooth muscle actin (α-SMA), **(B)** matrix metalloproteinase-1 (MMP-1), **(C)** interferon-γ (IFN-γ), **(D)** interleukin-8 (IL-8), **(E)** interleukin-2 (IL-2), **(F)** transforming growth factor-β (TGF-β), **(G)** fibroblast-specific protein-1 (FSP-1/S100A4), **(H)** collagen type I (COL1A1), **(I)** collagen type III (COL3A1), **(J)** vimentin and **(K)** macrophage inflammatory protein-1 (MIP-1). Data are presented as mean ± standard error of the mean (SEM). Statistical comparisons between groups were performed using a two-tailed unpaired Student's *t*-test in GraphPad Prism, with $P < 0.05$ considered statistically significant. Significance levels are indicated as $P < 0.05$, $P < 0.01$, $P < 0.001$, and $P < 0.0001$ (****); ns, not significant.

Supplementary file

Table S1. Summary of demographic characteristics, duration of diabetes, anatomical distribution of foot involvement, clinical manifestations, and associated comorbidities among 135 patients with DFU. Categorical variables are presented as frequencies and percentages; continuous variables are summarized using medians and interquartile ranges (IQRs).

Table S2. Clinical and microbiological characteristics of six diabetic foot ulcer cases (DF-01–DF-06), including age, sex, duration of diabetes, clinical diagnosis, bacterial identification by conventional culture, antimicrobial susceptibility profiles, random blood glucose, fasting blood glucose, glycated hemoglobin (HbA1c), and erythrocyte sedimentation rate (ESR).

Table S3. Summary of paired-end sequencing read counts and quality-control metrics obtained from five diabetic foot ulcer tissue specimens (DF_01–DF_05). The parameters include total read pairs, mean Phred quality scores, percentages of bases with quality scores greater than 30 (Q30), guanine–cytosine (GC) content, and read lengths for forward (R1) and reverse (R2) reads.

Table S4. Sample-specific Chao1 richness estimates and Shannon diversity indices calculated from 16S rRNA V3–V4 amplicon sequencing data obtained from five amputated diabetic foot ulcer tissue specimens (DF_01–DF_05). Chao1 provides an estimate of bacterial taxonomic richness; the Shannon diversity index incorporates both richness and the relative distribution of bacterial taxa. Chao1 estimates ranged from 67.75 to 272.00; Shannon diversity indices ranged from 0.48 to 4.39, indicating inter-sample variation in bacterial richness and community diversity.

Table S5. Forward and reverse primer sequences (5′–3′) used to assess the expression of inflammatory and immune-associated genes (IL2, CXCL8, IFN-Γ, and CCL3), extracellular matrix-remodeling gene MMP1, fibroblast- and myofibroblast-associated genes (TGFB1, ACTA2, S100A4, and VIM), and collagen-associated genes (COL1A1 and COL3A1). ACTB (β-actin) was used as the reference gene for normalization. All primer pairs were assigned an annealing temperature of 60 °C.

Declarations

Acknowledgements

The authors gratefully acknowledge Sri Balaji Vidyapeeth (Deemed to be University), Puducherry, for providing institutional support and research facilities. The authors also acknowledge the MVK Iyer Fellowship awarded to Maria Infant Majula Shifani Mahendran, Vaijayanthi Saravanan, and SivaSakthi Srikanth.

Funding

This research was supported by institutional SEED funding from Sri Balaji Vidyapeeth (Deemed to be University), Puducherry, India, under grant number SBV/IRC/SEED MONEY/196/2025.

Conflict of interest

The authors declare that they have no competing financial or non-financial interests.

Human ethics approval

The study was reviewed and approved by the Institutional Human Ethics Committee of Mahatma Gandhi Medical College & Research Institute, Sri Balaji Vidyapeeth (Deemed to be University), Puducherry (Approval No. MGMCRI/2024/02/IHEC/27). The study was conducted in accordance with ICMR 2019 guidelines

Consent to participate

Written informed consent was obtained from all study participants prior to sample collection.

Consent for publication

Consent for publication of the clinical information and images included in this study was obtained from the respective participants.

Data availability statement

The raw 16S rRNA sequencing data generated in this study have been deposited in the NCBI Sequence Read Archive (SRA) under BioProject accession number PRJNA1511977, with five associated BioSample accession numbers (SAMN64101525–SAMN64101529). The data are scheduled for public release in accordance with the NCBI release policy. Associated de-identified clinical data and supporting materials are publicly available in Figshare, and the Fig. related microbiome abundance data and associated R scripts used for 16S rRNA microbiome analysis and visualization are available in the GitHub repository: https://github.com/shifanimaju710-create/Diabetic-Foot-ulcer-16S-Microbiome-Analysis.

Clinical trial approval

N/A

Authors contributions

M.I.M.S. and V.G.: Conceptualization, methodology, investigation, formal analysis, data curation, experimental analysis, validation, visualization, supervision, project administration, writing -original draft preparation, and writing - review and editing. V.S.: Methodology, investigation, and writing - review and editing. P.J.: Clinical investigation, resources, and review. S.S.S.: investigation review and editing. C.H.G.M.: Scientific validation, interpretation of findings, and writing - review and editing. All authors have read and approved the final version of the manuscript.

Abbreviations

16S rRNA 16S ribosomal RNA

ACTA2/α-SMA Actin alpha 2 / alpha-smooth muscle actin

CAD Coronary Artery Disease

CKD Chronic kidney disease

COL-I Collagen type I

COL-III Collagen type III

CV Crystal Violet

DFU Diabetic Foot Ulcer

ECM Extracellular matrix

FSP-1 Fibroblast-specific protein 1

H&E Hematoxylin and eosin

IFN-γ Interferon gamma

IL Interleukin

IQR Interquartile range

MIP-1α/CCL3 Macrophage inflammatory protein-1 alpha / C-C motif chemokine ligand 3

MMP matrix metalloproteinase

MRSA Methicillin-resistant Staphylococcus aureus

OTU Operational Taxonomic Unit

PCoA Principal coordinate analysis

qPCR quantitative polymerase chain reaction

ROS reactive oxygen species

SEM Scanning electron microscopy

SHTN Systemic hypertension

TGF-β1, transforming growth factor beta 1

V3–V4 16S rRNA hypervariable region 3–4

References

1. Dawi J, Tumanyan K, Tomas K, Misakyan Y, Gargaloyan A, Gonzalez E, Hammi M, Tomas S, Venketaraman V (2025) Diabetic foot ulcers: pathophysiology, immune dysregulation, and emerging therapeutic strategies. Biomedicines 13:1076. https://doi.org/10.3390/biomedicines13051076
2. Mudrik-Zohar H, Carasso S, Gefen T, Zalmanovich A, Katzir M, Cohen Y, Paitan Y, Geva-Zatorsky N, Chowers M (2022) Microbiome characterization of infected diabetic foot ulcers in association with clinical outcomes: traditional cultures versus molecular sequencing methods. Front Cell Infect Microbiol 12:836699. https://doi.org/10.3389/fcimb.2022.836699
3. Dowd SE, Wolcott RD, Sun Y, McKeehan T, Smith E, Rhoads DD (2008) Polymicrobial nature of chronic diabetic foot ulcer biofilm infections determined using bacterial tag-encoded FLX amplicon pyrosequencing. PLoS One 3. https://doi.org/10.1371/journal.pone.0003326
4. Huang Y, Xiao Z, Cao Y, Gao F, Fu Y, Zou M, Luo X, Jiang Y, Xue Y (2022) Rapid microbiological diagnosis based on 16S rRNA gene sequencing: a comparison of bacterial composition in diabetic foot infections and contralateral intact skin. Front Microbiol 13:1021955. https://doi.org/10.3389/fmicb.2022.1021955
5. Dinh T, Tecilazich F, Kafanas A, Doupis J, Gnardellis C, Leal E, Tellechea A, Pradhan L, Lyons TE, Giurini JM, Veves A (2012) Mechanisms involved in the development and healing of diabetic foot ulceration. Diabetes 61:2937–2947. https://doi.org/10.2337/db12-0227
6. Srivastava P, Sondak T, Sivashanmugam K, Kim KS (2022) A review of immunomodulatory reprogramming by probiotics in combating chronic and acute diabetic foot ulcers (DFUs). Pharmaceutics 14:2436. https://doi.org/10.3390/pharmaceutics14112436
7. Ayuk SM, Abrahamse H, Houreld NN (2016) The role of matrix metalloproteinases in diabetic wound healing in relation to photobiomodulation. J Diabetes Res 2016:2897656. https://doi.org/10.1155/2016/2897656

8. Chen J, Qin S, Liu S, Zhong K, Jing Y, Wu X, Peng F, Li D, Peng C (2023) Targeting matrix metalloproteases in diabetic wound healing. Front Immunol 14:1089001. https://doi.org/10.3389/fimmu.2023.1089001
9. Piaggesi A, Viacava P, Rizzo L, Naccarato G, Baccetti F, Romanelli M, Zampa V, Del Prato S (2003) Semiquantitative analysis of the histopathological features of the neuropathic foot ulcer: effects of pressure relief. Diabetes Care 26:3123–3128. https://doi.org/10.2337/diacare.26.11.3123
10. Kundu D, Jayaraman A, Sen CK (2026) Clinical measurement of transepidermal water loss. Adv Wound Care (New Rochelle) 15:73–90. https://doi.org/10.1089/wound.2024.0148
11. Chattopadhyay D, Sinha M, Kapoor A, Kumar M, Singh K, Mathew-Steiner SS, Sen CK (2024) Deficient functional wound closure as measured by elevated trans-epidermal water loss predicts chronic wound recurrence: an exploratory observational study. Sci Rep 14:23593. https://doi.org/10.1038/s41598-024-74426-0
12. Kalan LR, Brennan MB (2019) The role of the microbiome in nonhealing diabetic wounds. Ann N Y Acad Sci 1435:79–92. https://doi.org/10.1111/nyas.13926
13. Malone M, Johani K, Jensen SO, Gosbell IB, Dickson HG, Hu H, Vickery K (2017) Next generation DNA sequencing of tissues from infected diabetic foot ulcers. EBioMedicine 21:142–149. https://doi.org/10.1016/j.ebiom.2017.06.026
14. Pouget C, Dunyach-Remy C, Pantel A, Schuldiner S, Sotto A, Lavigne JP (2020) Biofilms in diabetic foot ulcers: significance and clinical relevance. Microorganisms 8:1580. https://doi.org/10.3390/microorganisms8101580
15. James GA, Swogger E, Wolcott R, Pulcini E, Secor P, Sestrich J, Costerton JW, Stewart PS (2008) Biofilms in chronic wounds. Wound Repair Regen 16:37–44. https://doi.org/10.1111/j.1524-475X.2007.00321.x
16. Neut D, van Horn JR, van Kooten TG, van der Mei HC, Busscher HJ (2011) Biofilms in chronic diabetic foot ulcers: a study of two cases. Acta Orthop 82:383–385. https://doi.org/10.3109/17453674.2011.588861
17. Liu Y, Long S, Wang H, Wang Y (2024) Biofilm therapy for chronic wounds. Int Wound J 21. https://doi.org/10.1111/iwj.14667
18. Lichtenberg M, Kirketerp-Møller K, Kvich LA, Christensen MH, Fritz B, Jakobsen TH, Bjarnsholt T (2024) Single cells and bacterial biofilm populations in chronic wound infections. APMIS 132:1071–1077. https://doi.org/10.1111/apm.13344
19. Michaelis C, Grohmann E (2023) Horizontal gene transfer of antibiotic resistance genes in biofilms. Antibiotics (Basel) 12:328. https://doi.org/10.3390/antibiotics12020328
20. Lavery LA, Bhavan K, Wukich DK (2019) Biofilm and diabetic foot ulcer healing: all hat and no cattle. Ann Transl Med 7(Suppl 6). https://doi.org/10.21037/atm.2019.09.09
21. Theocharidis G et al (2020) Integrated skin transcriptomics and serum multiplex assays reveal novel mechanisms of wound healing in diabetic foot ulcers. Diabetes 69:2157–2169. https://doi.org/10.2337/db20-0188

22. Hassan N, Ilyas A, Memon MF, Shafiq Y, Zahra SI, Arif A, Nawab SN (2026) Gene expression analysis of diabetic foot ulcers reveals the potential impact of levofloxacin on wound healing. Sci Rep 16:3832. https://doi.org/10.1038/s41598-025-33932-5
23. Littig JPB, Moellmer R, Estes AM, Agrawal DK, Rai V (2022) Increased population of CD40+ fibroblasts is associated with impaired wound healing and chronic inflammation in diabetic foot ulcers. J Clin Med 11:6335. https://doi.org/10.3390/jcm11216335
24. Maione AG, Smith A, Kashpur O, Yanez V, Knight E, Mooney DJ, Veves A, Tomic-Canic M, Garlick JA (2016) Altered extracellular matrix deposition by diabetic foot ulcer-derived fibroblasts implicates fibronectin in chronic wound repair. Wound Repair Regen 24:630–643. https://doi.org/10.1111/wrr.12437
25. Sawaya AP et al (2020) Deregulated immune cell recruitment orchestrated by FOXM1 impairs human diabetic wound healing. Nat Commun 11:4678. https://doi.org/10.1038/s41467-020-18276-0
26. Bolyen E et al (2019) Reproducible, interactive, scalable and extensible microbiome data science using QIIME 2. Nat Biotechnol 37:852–857. https://doi.org/10.1038/s41587-019-0209-9
27. Rognes T, Flouri T, Nichols B, Quince C, Mahé F (2016) VSEARCH: a versatile open-source tool for metagenomics. PeerJ 4. https://doi.org/10.7717/peerj.2584
28. Quast C, Pruesse E, Yilmaz P, Gerken J, Schweer T, Yarza P, Peplies J, Glöckner FO (2013) The SILVA ribosomal RNA gene database project: improved data processing and web-based tools. Nucleic Acids Res 41–D596. https://doi.org/10.1093/nar/gks1219
29. Gopalakrishnan V, Mahendran MIMS, Saravanan V, Ramaswamy D (2025) Transcriptional modulation of *Porphyromonas gingivalis* biofilms on titanium-copper implant surfaces. Folia Microbiol (Praha) 70:1345–1357. https://doi.org/10.1007/s12223-025-01246-8
30. Gopalakrishnan V, Saxena P, Thakur P, Lipatov A, Sani RK (2024) Impact of graphene layers on genetic expression and regulation within sulfate-reducing biofilms. Microorganisms 12:1759. https://doi.org/10.3390/microorganisms12091759
31. O'Toole GA (2011) Microtiter dish biofilm formation assay. J Vis Exp 47. https://doi.org/10.3791/2437
32. Fischer ER, Hansen BT, Nair V, Hoyt FH, Schwartz CL, Dorward DW (2024) Scanning electron microscopy. Curr Protoc 4. https://doi.org/10.1002/cpz1.1034
33. Livak KJ, Schmittgen TD (2001) Analysis of relative gene expression data using real-time quantitative PCR and the 2^−ΔΔCT method. Methods 25:402–408. https://doi.org/10.1006/meth.2001.1262
34. Kalan LR, Brennan MB (2019) The role of the microbiome in nonhealing diabetic wounds. Ann N Y Acad Sci 1435:79–92. https://doi.org/10.1111/nyas.13926
35. Loesche M et al (2017) Temporal stability in chronic wound microbiota is associated with poor healing. J Invest Dermatol 137:237–244. https://doi.org/10.1016/j.jid.2016.08.009
36. Johani K et al (2017) Microscopy visualization confirms multi-species biofilms are ubiquitous in diabetic foot ulcers. Int Wound J 14:1160–1169. https://doi.org/10.1111/iwj.12777
37. Kalan LR et al (2019) Strain- and species-level variation in the microbiome of diabetic wounds is associated with clinical outcomes and therapeutic efficacy. Cell Host Microbe 25:641–655.e5. https://doi.org/10.1016/j.chom.2019.03.006

38. Villa F, Marchandin H, Lavigne JP, Schuldiner S, Cellier N, Sotto A, Loubet P (2024) Anaerobes in diabetic foot infections: pathophysiology, epidemiology, virulence, and management. Clin Microbiol Rev 37. https://doi.org/10.1128/cmr.00143-23
39. Voza FA et al (2024) Fibroblasts in diabetic foot ulcers. Int J Mol Sci 25:2172. https://doi.org/10.3390/ijms25042172
40. Rai V, Moellmer R, Agrawal DK (2022) The role of CXCL8 in chronic nonhealing diabetic foot ulcers and phenotypic changes in fibroblasts: a molecular perspective. Mol Biol Rep 49:1565–1572. https://doi.org/10.1007/s11033-022-07144-3
41. Chen R, Zou L (2024) Combined analysis of single-cell sequencing and bulk transcriptome sequencing reveals new mechanisms for non-healing diabetic foot ulcers. PLoS One 19. https://doi.org/10.1371/journal.pone.0306248
42. Zheng G et al (2010) Phenotypic and molecular characterization of *Solobacterium moorei* isolates from patients with wound infection. J Clin Microbiol 48:873–876. https://doi.org/10.1128/JCM.01381-09
43. Dinh T, Tecilazich F, Kafanas A, Doupis J, Gnardellis C, Leal E, Tellechea A, Pradhan L, Lyons TE, Giurini JM, Veves A (2012) Mechanisms involved in the development and healing of diabetic foot ulceration. Diabetes 61:2937–2947. https://doi.org/10.2337/db12-0227
44. Alauzet C et al (2021) A new look at the genus *Solobacterium*: a retrospective analysis of twenty-seven cases of infection involving *S. moorei* and a review of sequence databases and the literature. Microorganisms 9:1229. https://doi.org/10.3390/microorganisms9061229

Fig. 1

A)



B)



C)



D)



E)



Fig. 2

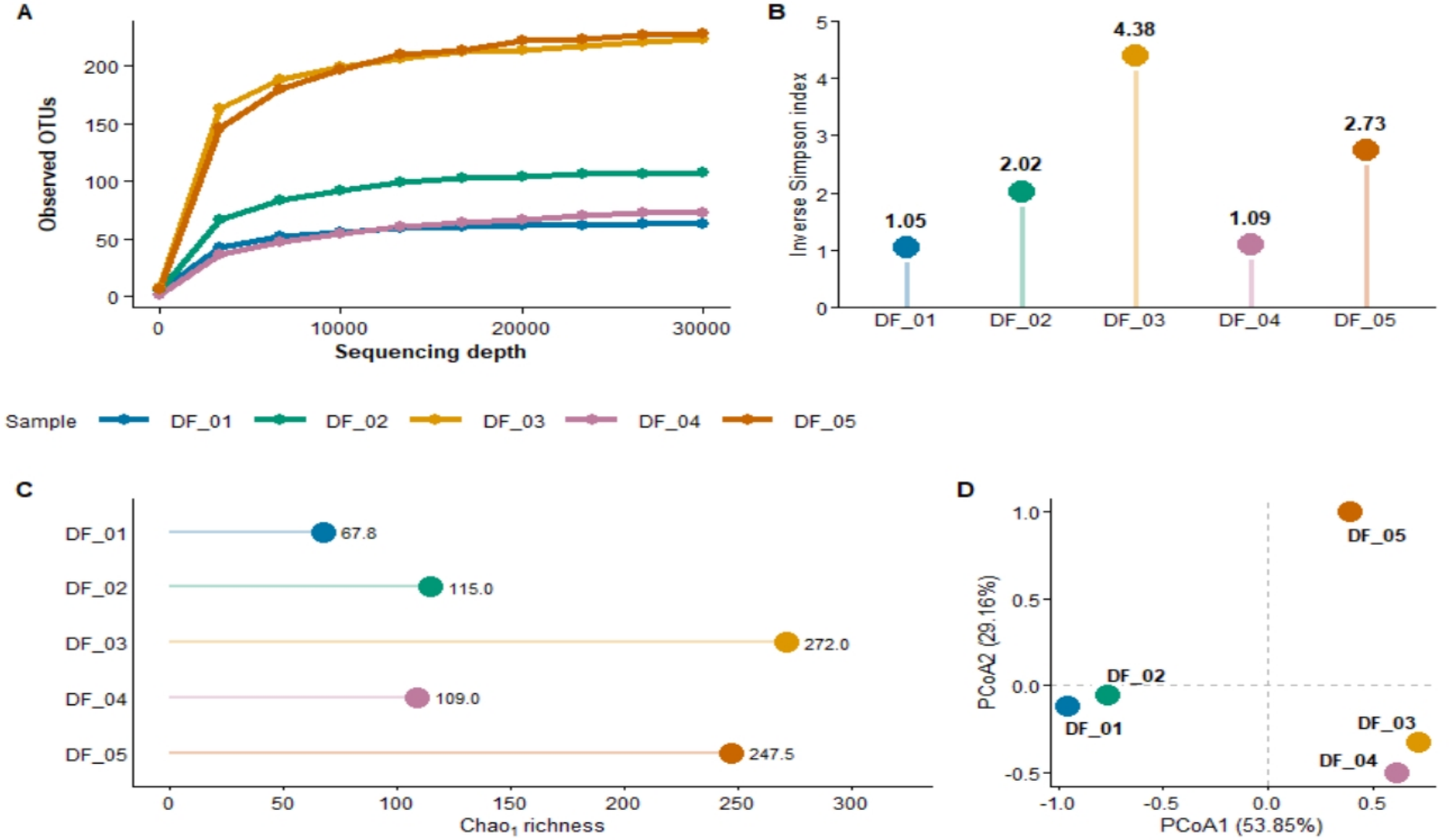

A
Observed OTUs
Sequencing depth
Sample
DF_01
DF_02
DF_03
DF_04
DF_05
B
Inverse Simpson index
1.05
2.02
4.38
1.09
2.73
C
67.8
115.0
272.0
109.0
247.5
Chao1 richness
D
PCoA2 (29.16%)
PCoA1 (53.85%)

Fig. 3

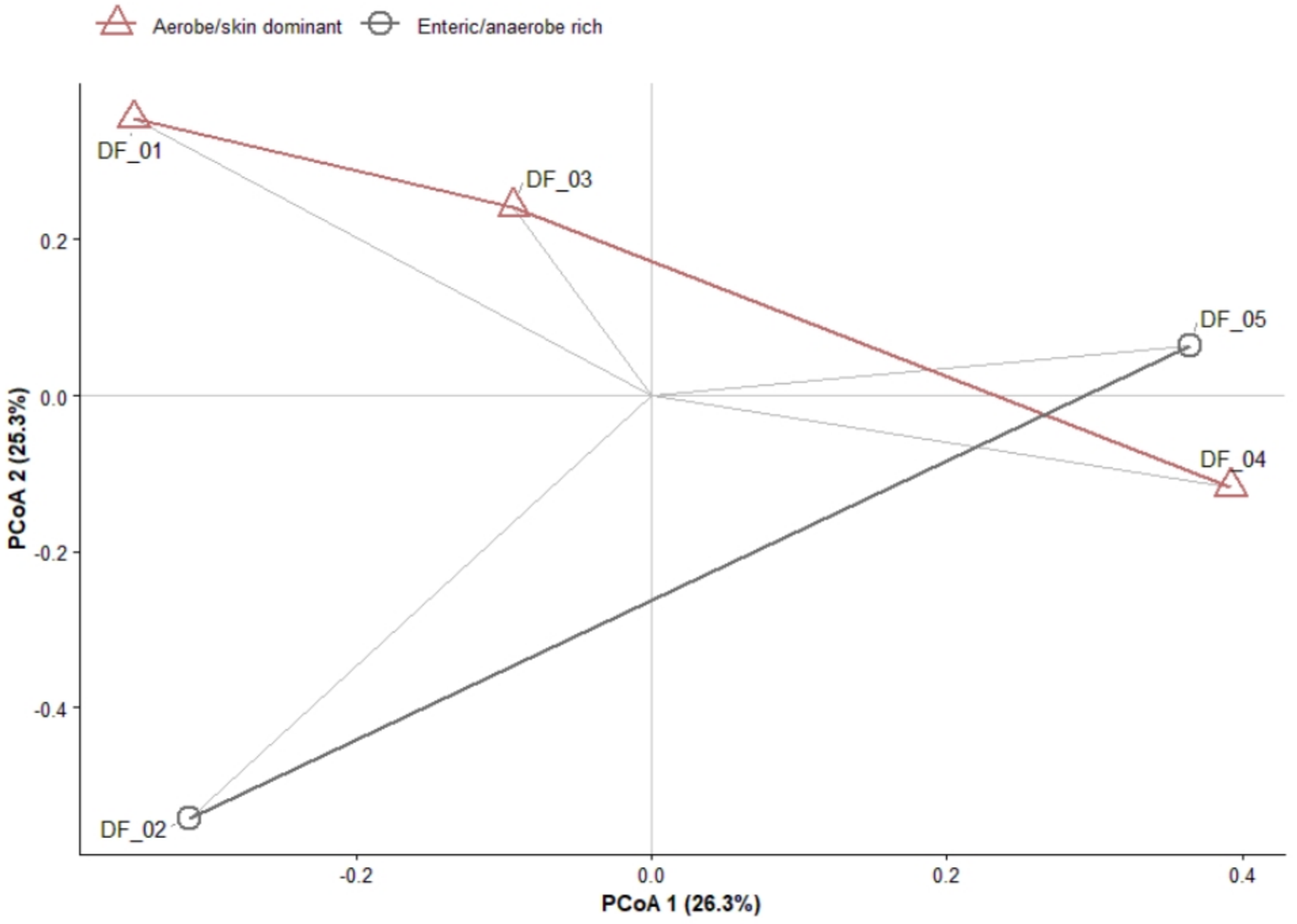

Aerobe/skin dominant
Enteric/anaerobe rich
DF_01
DF_03
DF_05
DF_04
DF_02
0.2
0.0
-0.2
-0.4
PCoA 2 (25.3%)
-0.2
0.0
0.2
0.4
PCoA 1 (26.3%)

Fig. 4

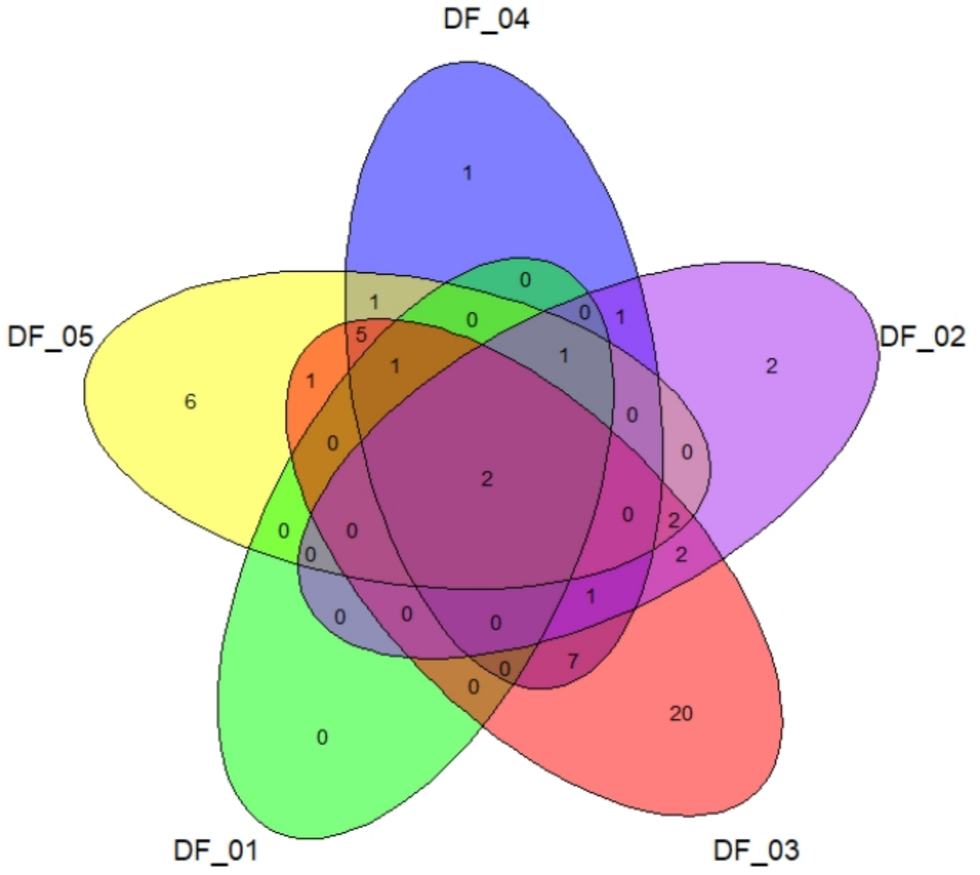

DF_04
DF_05
DF_02
DF_01
DF_03
1
6
2
0
20
1
0
1
0
1
5
1
1
1
0
0
0
2
0
0
0
2
0
2
0
0
0
1
0
0
0
0
7
0

Fig. 5

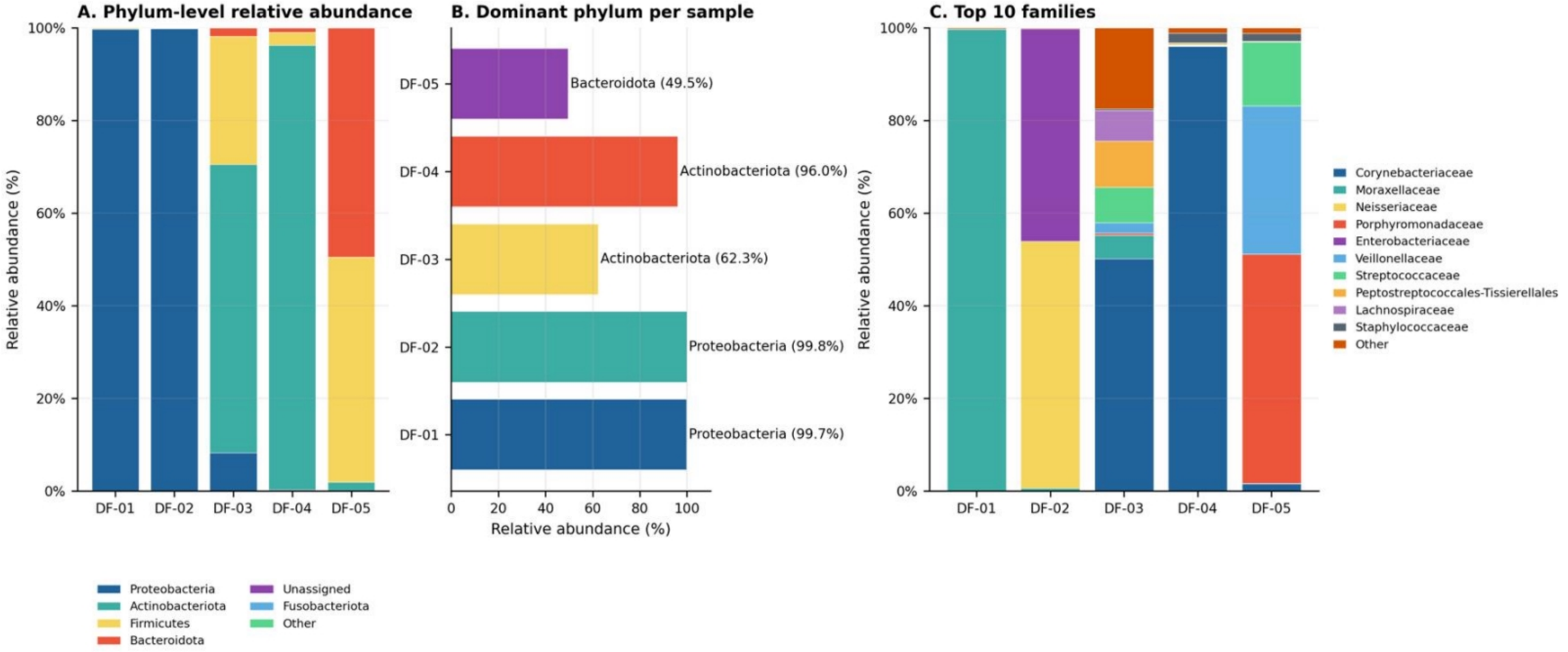

A. Phylum-level relative abundance
Relative abundance (%)
100%
80%
60%
40%
20%
0%
DF-01
DF-02
DF-03
DF-04
DF-05
Proteobacteria
Actinobacteriota
Firmicutes
Bacteroidota
Unassigned
Fusobacteriota
Other
B. Dominant phylum per sample
DF-05
Bacteroidota (49.5%)
DF-04
Actinobacteriota (96.0%)
DF-03
Actinobacteriota (62.3%)
DF-02
Proteobacteria (99.8%)
DF-01
Proteobacteria (99.7%)
0
20
40
60
80
100
Relative abundance (%)
C. Top 10 families
Relative abundance (%)
Corynebacteriaceae
Moraxellaceae
Neisseriaceae
Porphyromonadaceae
Enterobacteriaceae
Veillonellaceae
Streptococcaceae
Peptostreptococcales-Tissierellales
Lachnospiraceae
Staphylococcaceae
Other

Fig. 6

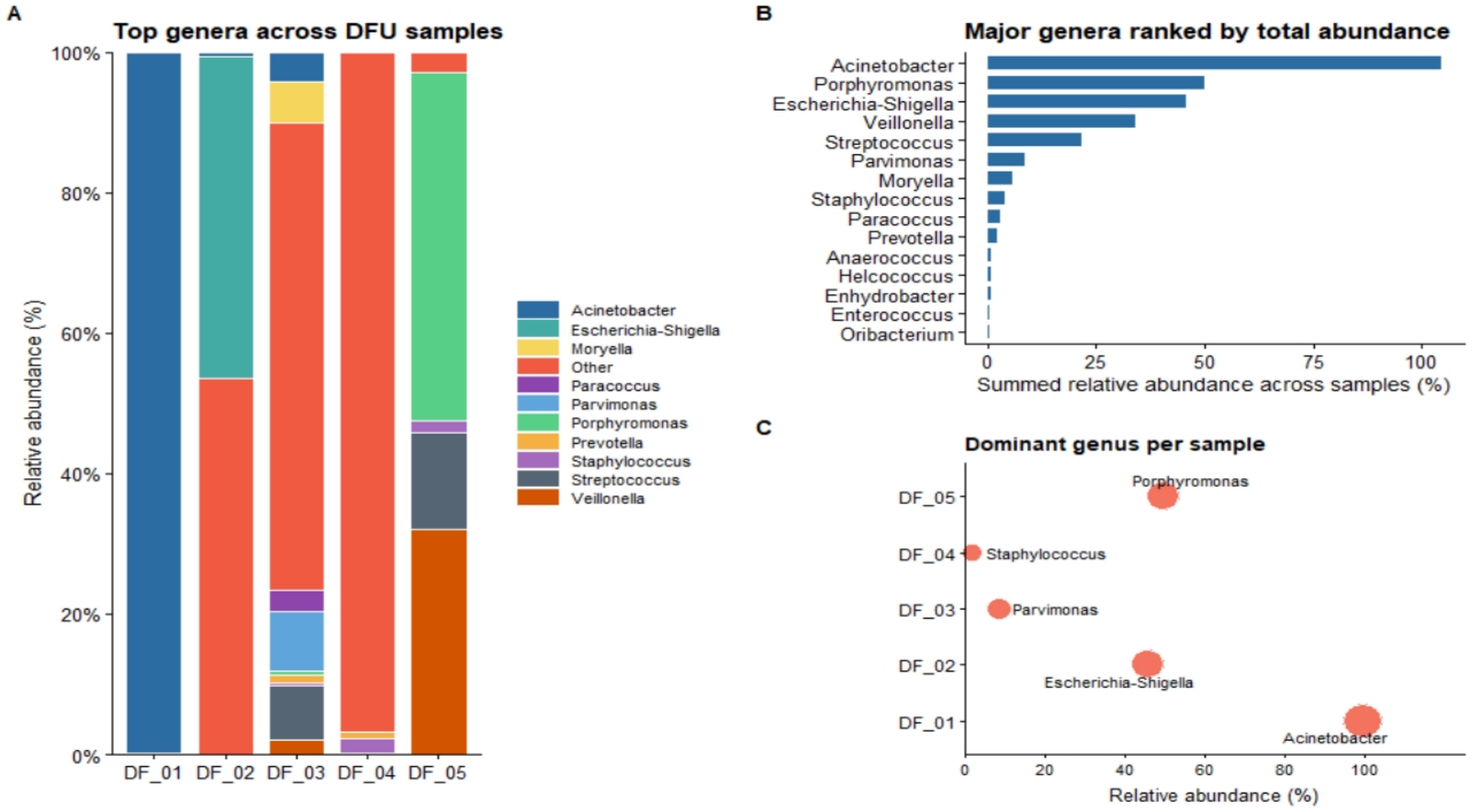

A
Top genera across DFU samples
Relative abundance (%)
100%
80%
60%
40%
20%
0%
DF_01
DF_02
DF_03
DF_04
DF_05
Acinetobacter
Escherichia-Shigella
Moryella
Other
Paracoccus
Parvimonas
Porphyromonas
Prevotella
Staphylococcus
Streptococcus
Veillonella
B
Major genera ranked by total abundance
Acinetobacter
Porphyromonas
Escherichia-Shigella
Veillonella
Streptococcus
Parvimonas
Moryella
Staphylococcus
Paracoccus
Prevotella
Anaerococcus
Helcococcus
Enhydrobacter
Enterococcus
Oribacterium
0
25
50
75
100
Summed relative abundance across samples (%)
C
Dominant genus per sample
DF_05
DF_04
DF_03
DF_02
DF_01
Porphyromonas
Staphylococcus
Parvimonas
Escherichia-Shigella
Acinetobacter
0
20
40
60
80
100
Relative abundance (%)

Fig. 7

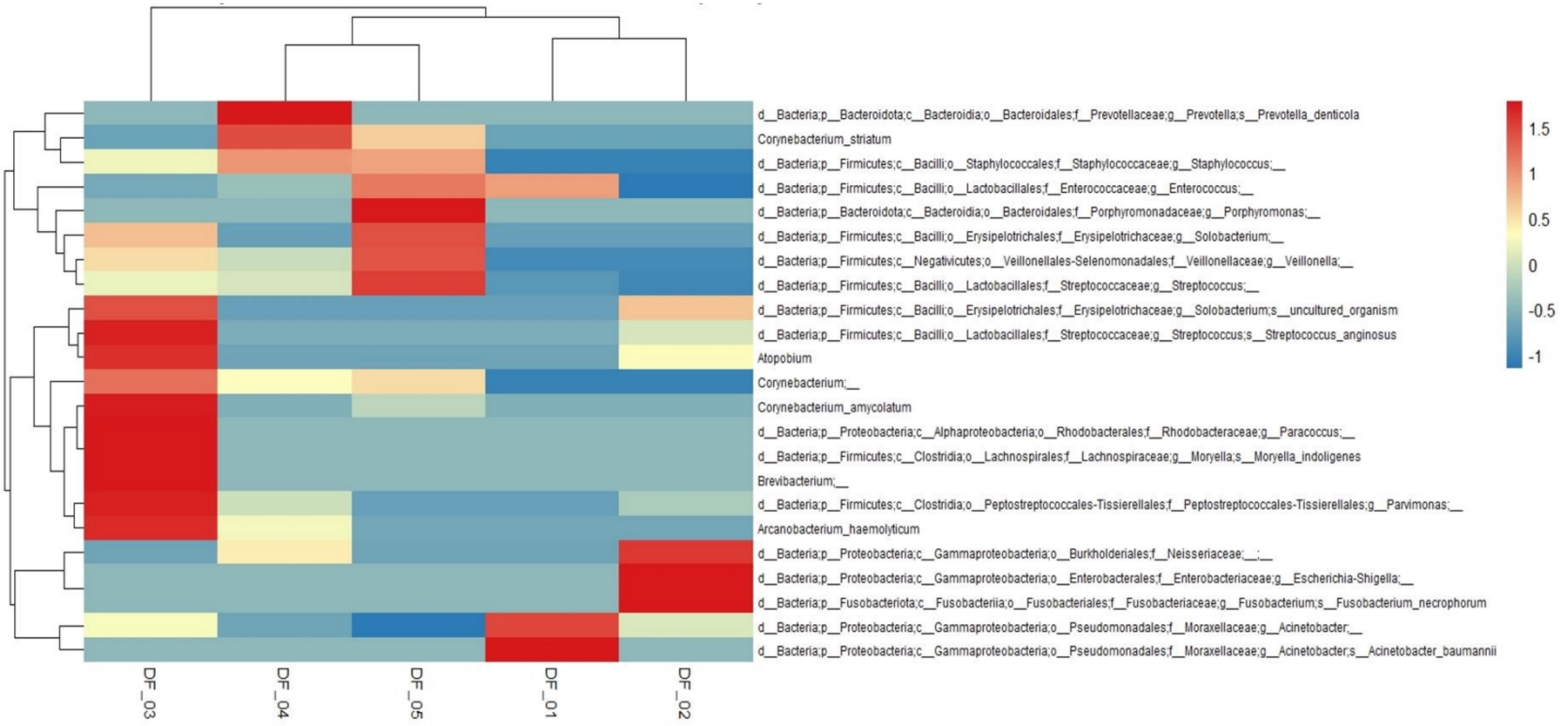

d__Bacteria;p__Bacteroidota;c__Bacteroidia;o__Bacteroidales;f__Prevotellaceae;g__Prevotella;s__Prevotella_denticola
Corynebacterium_striatum
d__Bacteria;p__Firmicutes;c__Bacilli;o__Staphylococcales;f__Staphylococcaceae;g__Staphylococcus;__
d__Bacteria;p__Firmicutes;c__Bacilli;o__Lactobacillales;f__Enterococcaceae;g__Enterococcus;__
d__Bacteria;p__Bacteroidota;c__Bacteroidia;o__Bacteroidales;f__Porphyromonadaceae;g__Porphyromonas;__
d__Bacteria;p__Firmicutes;c__Bacilli;o__Erysipelotrichales;f__Erysipelotrichaceae;g__Solobacterium;__
d__Bacteria;p__Firmicutes;c__Negativicutes;o__Veillonellales-Selenomonadales;f__Veillonellaceae;g__Veillonella;__
d__Bacteria;p__Firmicutes;c__Bacilli;o__Lactobacillales;f__Streptococcaceae;g__Streptococcus;__
d__Bacteria;p__Firmicutes;c__Bacilli;o__Erysipelotrichales;f__Erysipelotrichaceae;g__Solobacterium;s__uncultured_organism
d__Bacteria;p__Firmicutes;c__Bacilli;o__Lactobacillales;f__Streptococcaceae;g__Streptococcus;s__Streptococcus_anginosus
Atopobium
Corynebacterium;__
Corynebacterium_amycolatum
d__Bacteria;p__Proteobacteria;c__Alphaproteobacteria;o__Rhodobacterales;f__Rhodobacteraceae;g__Paracoccus;__
d__Bacteria;p__Firmicutes;c__Clostridia;o__Lachnospirales;f__Lachnospiraceae;g__Moryella;s__Moryella_indoligenes
Brevibacterium;__
d__Bacteria;p__Firmicutes;c__Clostridia;o__Peptostreptococcales-Tissierellales;f__Peptostreptococcales-Tissierellales;g__Parvimonas;__
Arcanobacterium_haemolyticum
d__Bacteria;p__Proteobacteria;c__Gammaproteobacteria;o__Burkholderiales;f__Neisseriaceae;__;__
d__Bacteria;p__Proteobacteria;c__Gammaproteobacteria;o__Enterobacterales;f__Enterobacteriaceae;g__Escherichia-Shigella;__
d__Bacteria;p__Fusobacteriota;c__Fusobacteriia;o__Fusobacteriales;f__Fusobacteriaceae;g__Fusobacterium;s__Fusobacterium_necrophorum
d__Bacteria;p__Proteobacteria;c__Gammaproteobacteria;o__Pseudomonadales;f__Moraxellaceae;g__Acinetobacter;__
d__Bacteria;p__Proteobacteria;c__Gammaproteobacteria;o__Pseudomonadales;f__Moraxellaceae;g__Acinetobacter;s__Acinetobacter_baumannii
DF_03
DF_04
DF_05
DF_01
DF_02
1.5
1
0.5
0
-0.5
-1

Fig. 8

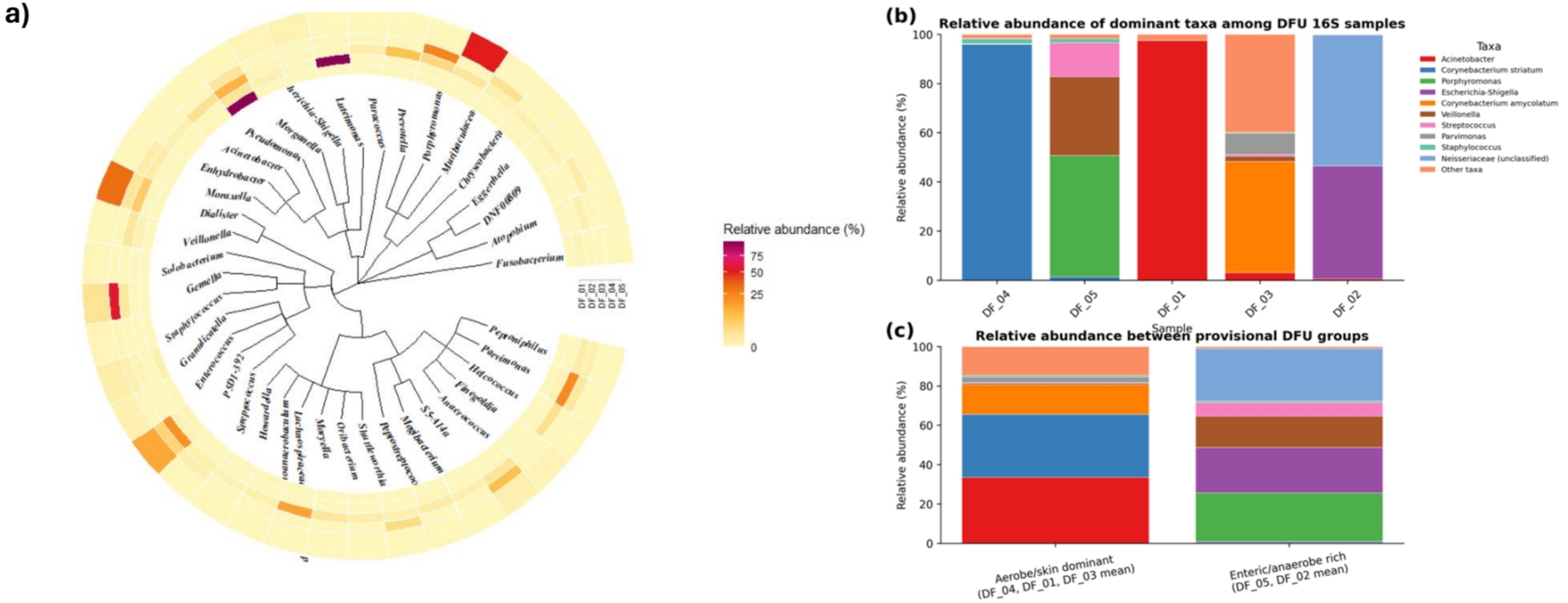

a)
Relative abundance (%)
75
50
25
0
DF_01
DF_02
DF_03
DF_04
DF_05
Escherichia-Shigella
Lutetimonas
Paracoccus
Prevotella
Porphyromonas
Muribaculaceae
Chryseobacterium
Eggerthella
DNF00809
Atopobium
Fusobacterium
Peptoniphilus
Parvimonas
Hoyosella
Finegoldia
Anaerococcus
SS-A14a
Megasphaera
Peptostreptococcus
Shuttleworthia
Oribacterium
Moryella
Lachnoanaerobaculum
Howardella
Streptococcus
P-SD1-392
Enterococcus
Granulicatella
Staphylococcus
Gemella
Solobacterium
Veillonella
Dialister
Moraxella
Enhydrobacter
Acinetobacter
Pseudomonas
Morganella
b)
Relative abundance of dominant taxa among DFU 16S samples
Relative abundance (%)
Sample
DF_04
DF_05
DF_01
DF_03
DF_02
Taxa
Acinetobacter
Corynebacterium striatum
Porphyromonas
Escherichia-Shigella
Corynebacterium amycolatum
Veillonella
Streptococcus
Parvimonas
Staphylococcus
Neisseriaceae (unclassified)
Other taxa
c)
Relative abundance between provisional DFU groups
Relative abundance (%)
Aerobe/skin dominant
(DF_04, DF_01, DF_03 mean)
Enteric/anaerobe rich
(DF_05, DF_02 mean)

Fig. 9

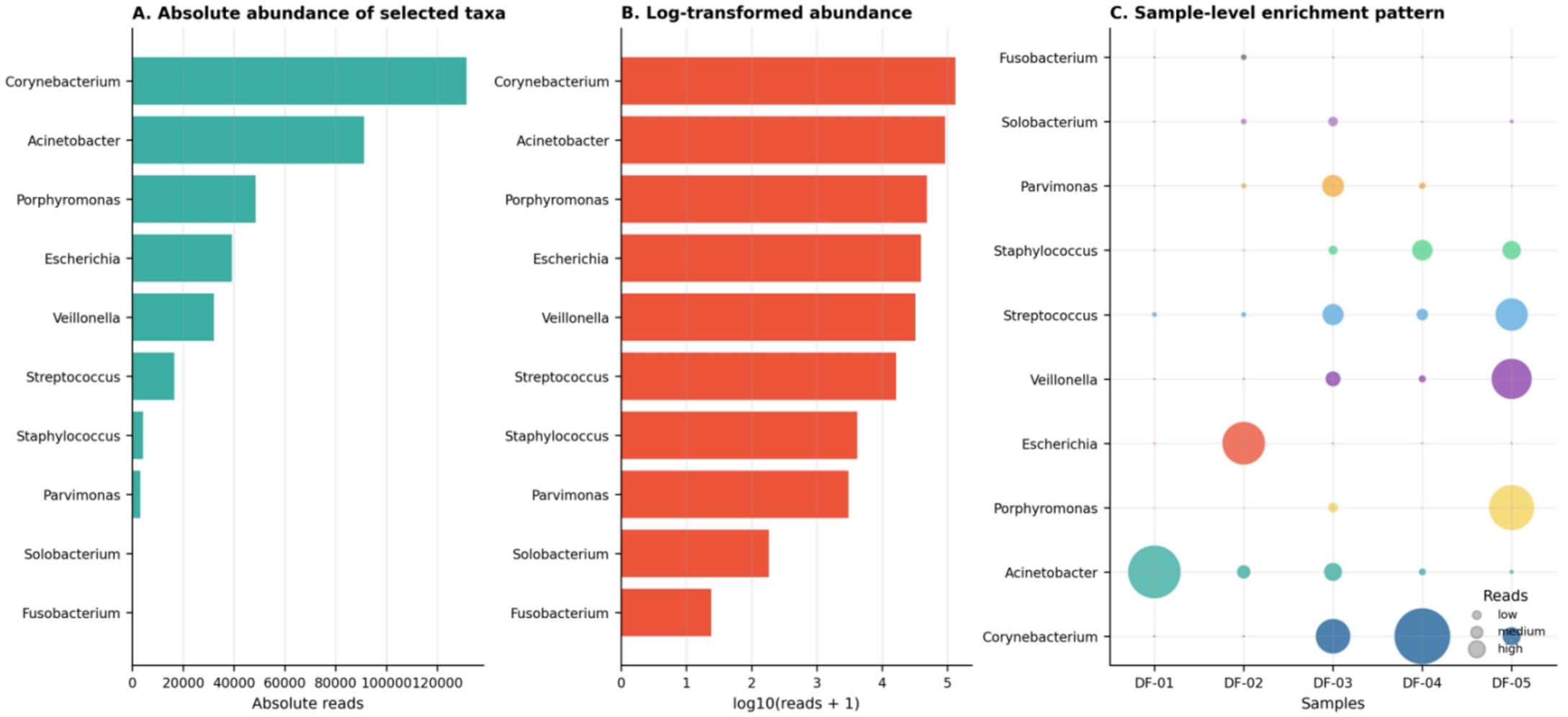

A. Absolute abundance of selected taxa
Corynebacterium
Acinetobacter
Porphyromonas
Escherichia
Veillonella
Streptococcus
Staphylococcus
Parvimonas
Solobacterium
Fusobacterium
0
20000
40000
60000
80000
100000
120000
Absolute reads
B. Log-transformed abundance
Corynebacterium
Acinetobacter
Porphyromonas
Escherichia
Veillonella
Streptococcus
Staphylococcus
Parvimonas
Solobacterium
Fusobacterium
0
1
2
3
4
5
log10(reads + 1)
C. Sample-level enrichment pattern
Fusobacterium
Solobacterium
Parvimonas
Staphylococcus
Streptococcus
Veillonella
Escherichia
Porphyromonas
Acinetobacter
Corynebacterium
Reads
low
medium
high
DF-01
DF-02
DF-03
DF-04
DF-05
Samples

Fig. 10

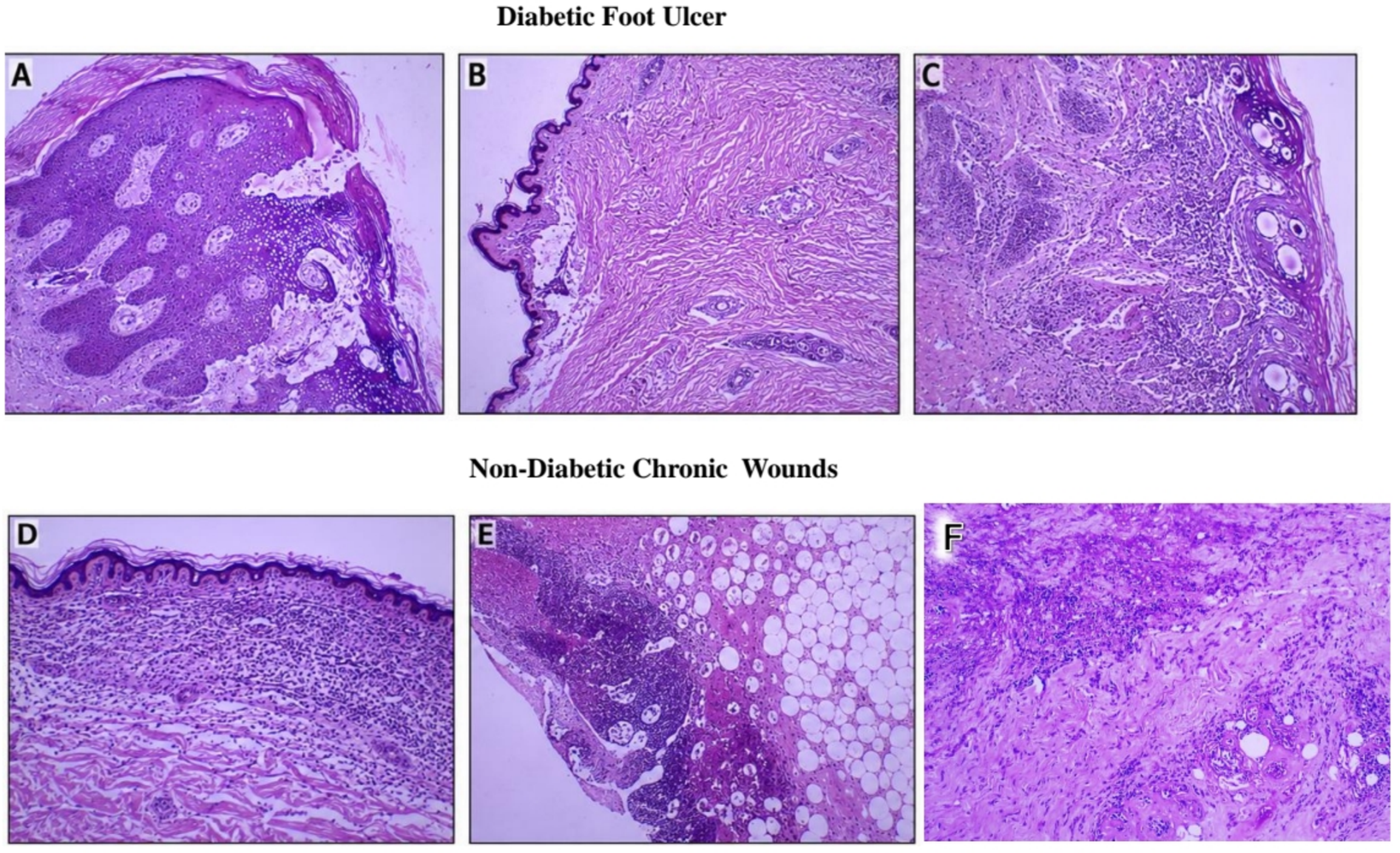
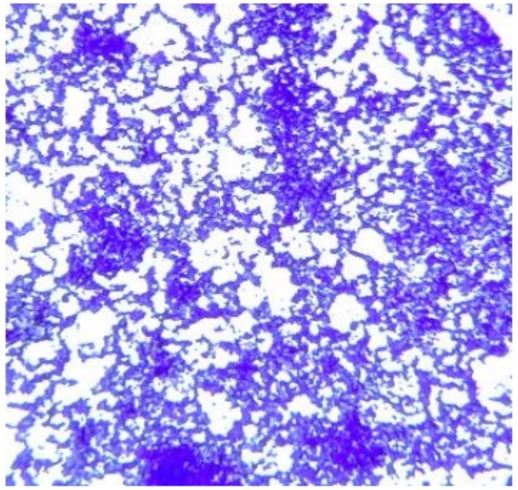


Fig. 11

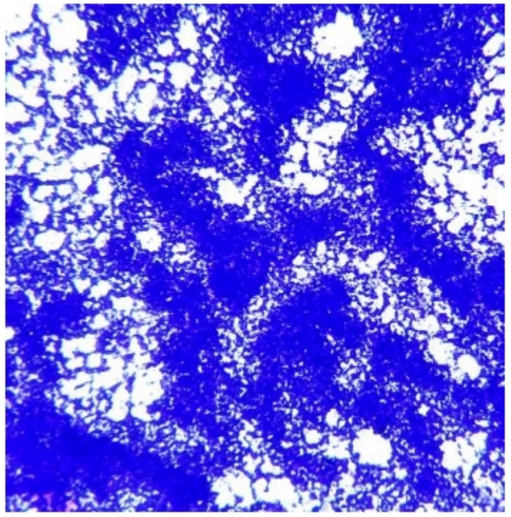
A)

6hrs



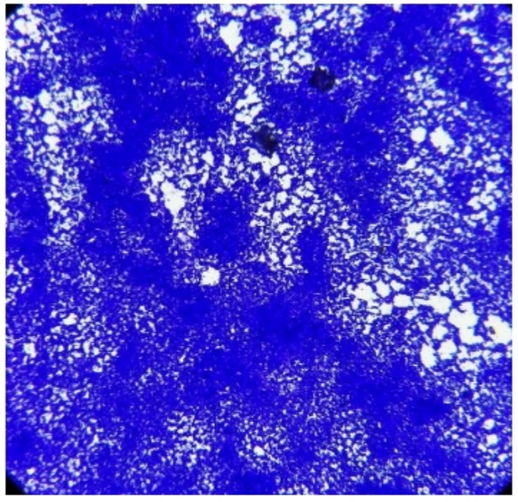
B)

12hrs



C)

24hrs



D)

48hrs

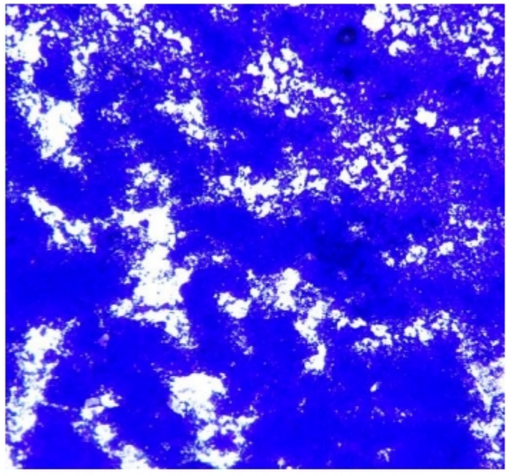
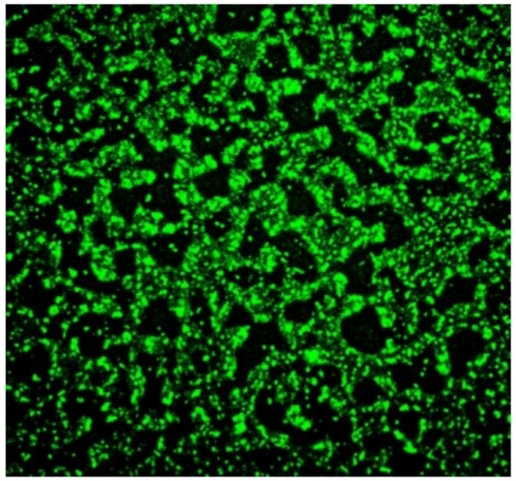


Fig. 12

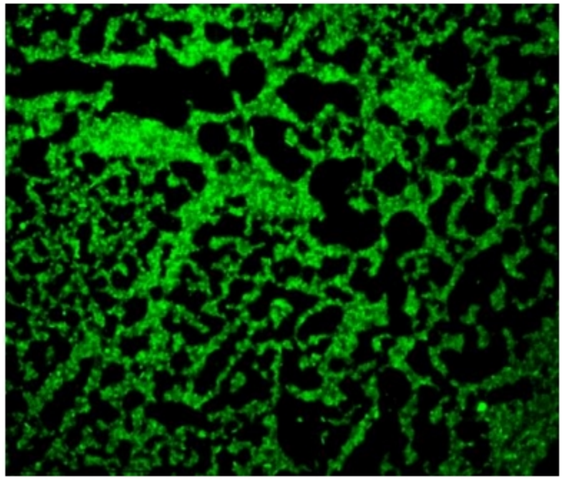
6hrs

A)



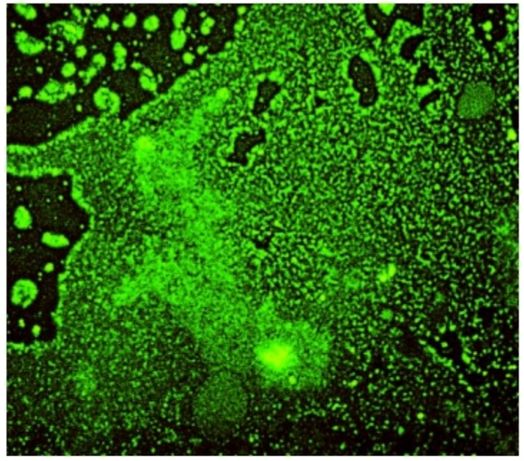
12hrs

B)



24hrs

C)



48hrs

D)

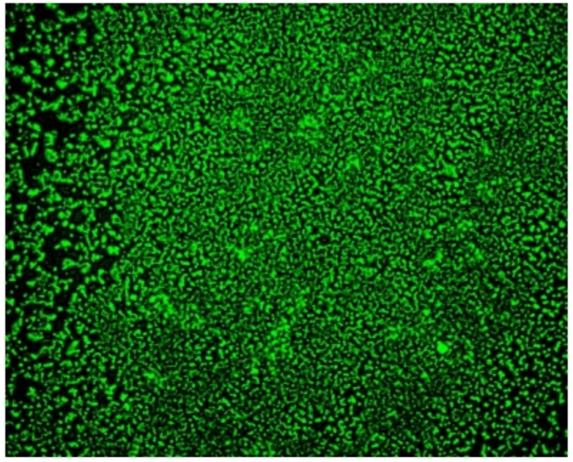
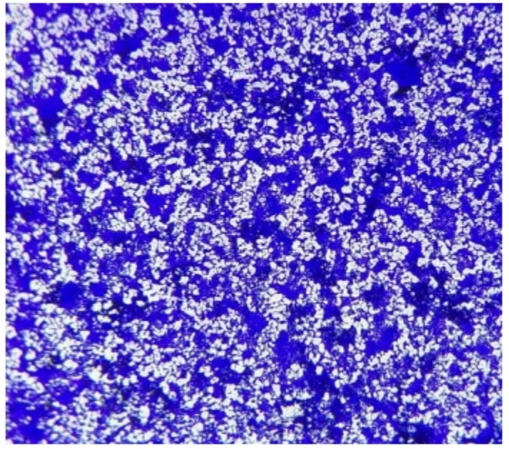


Fig. 13

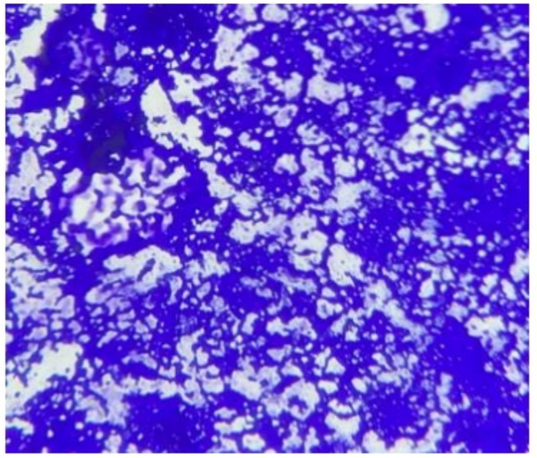
A)

6hrs



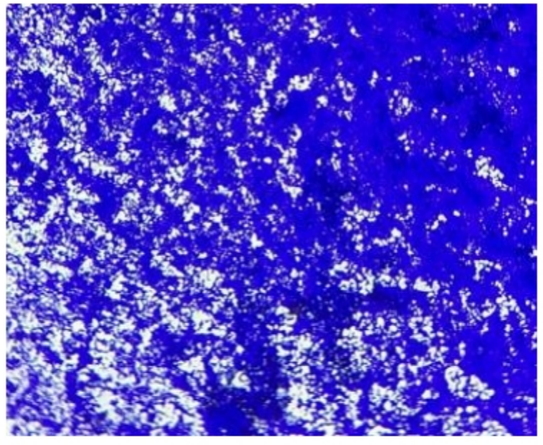
B)

12hrs



C)

24hrs



D)

48hrs

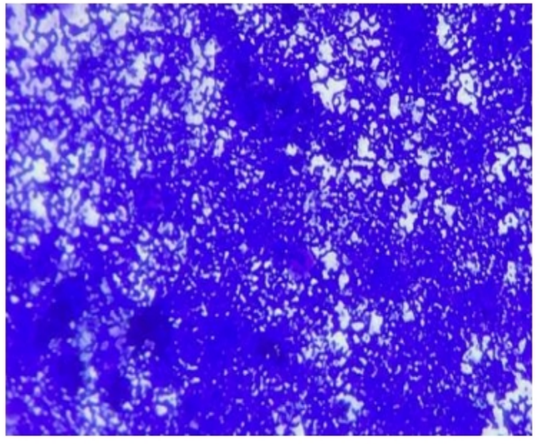


Fig. 14

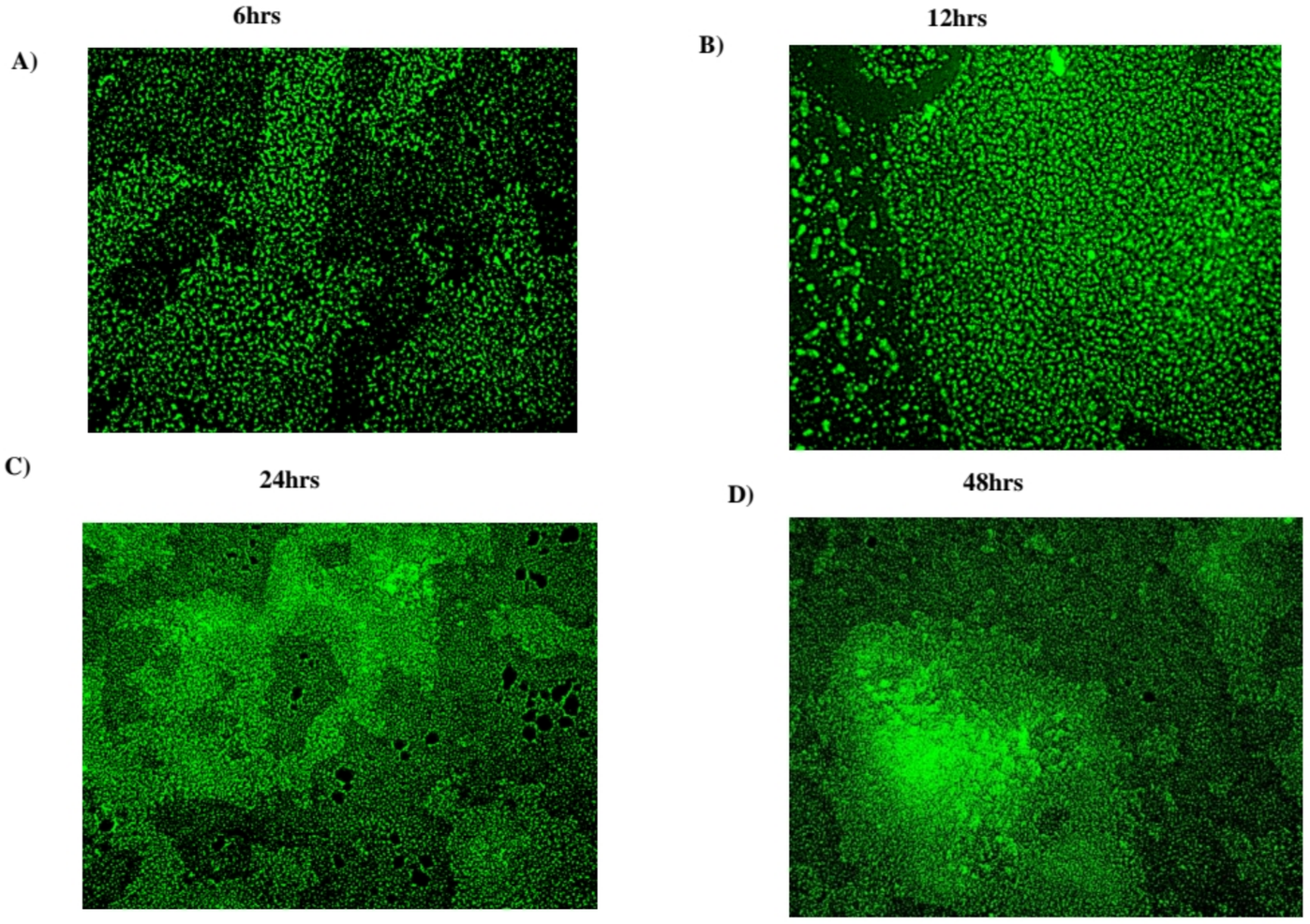
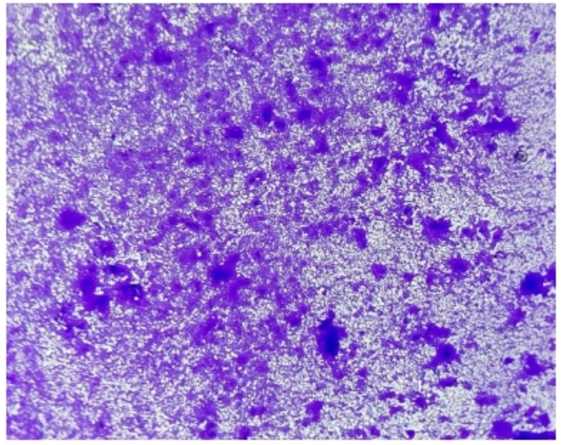


Fig. 15

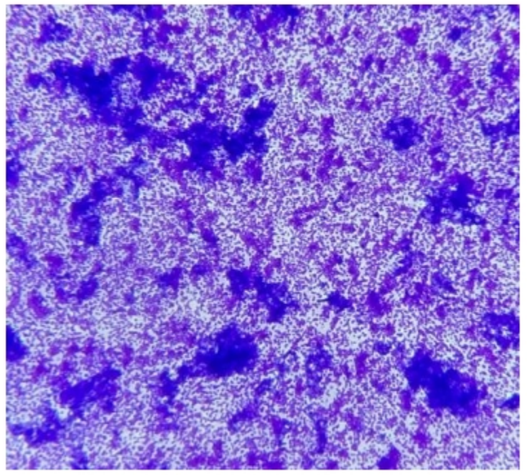
A)

2nd day



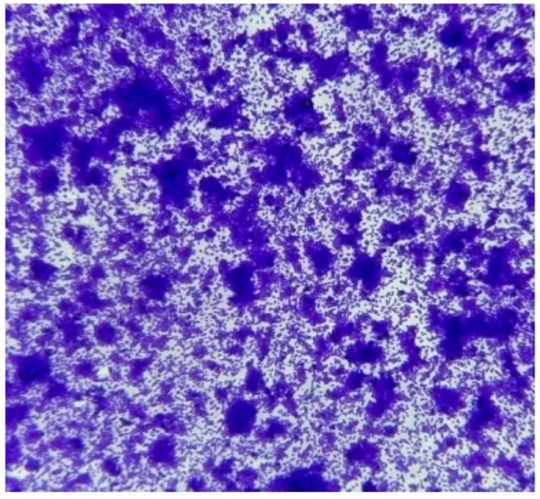
B)

4th day



C)

8th day



D)

16th day

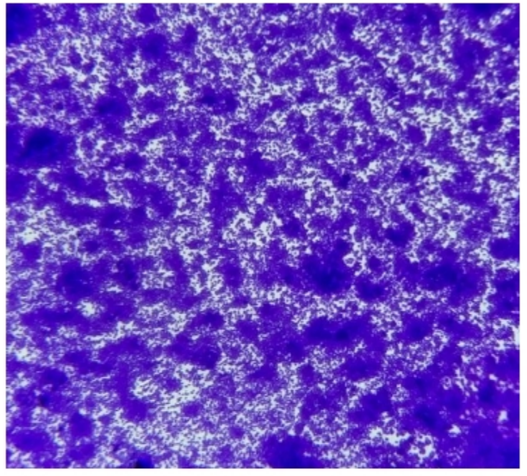
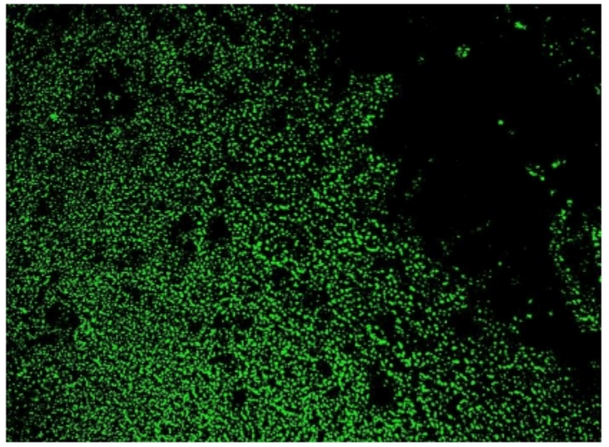
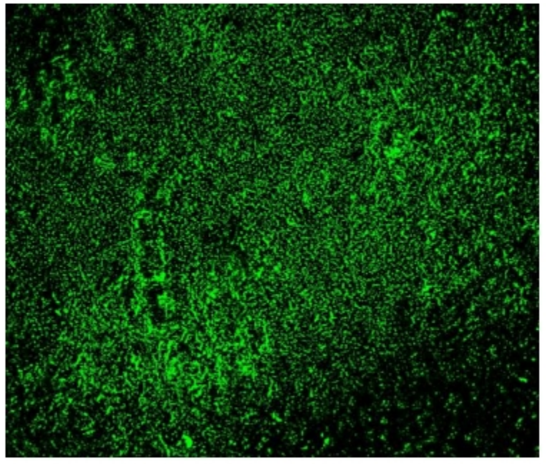


Fig. 16

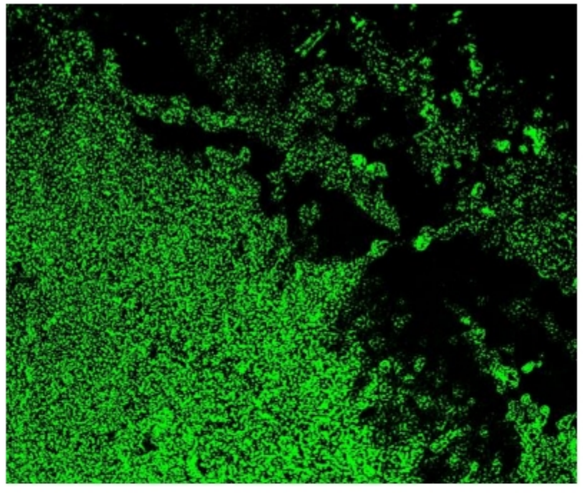
A) 2nd day



B) 4th day



C) 8th day



D) 16th day

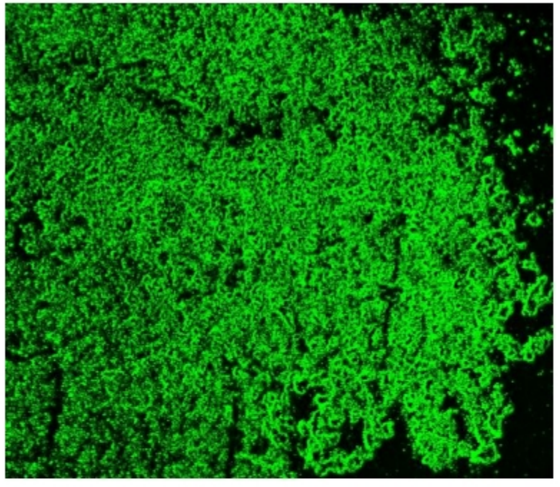
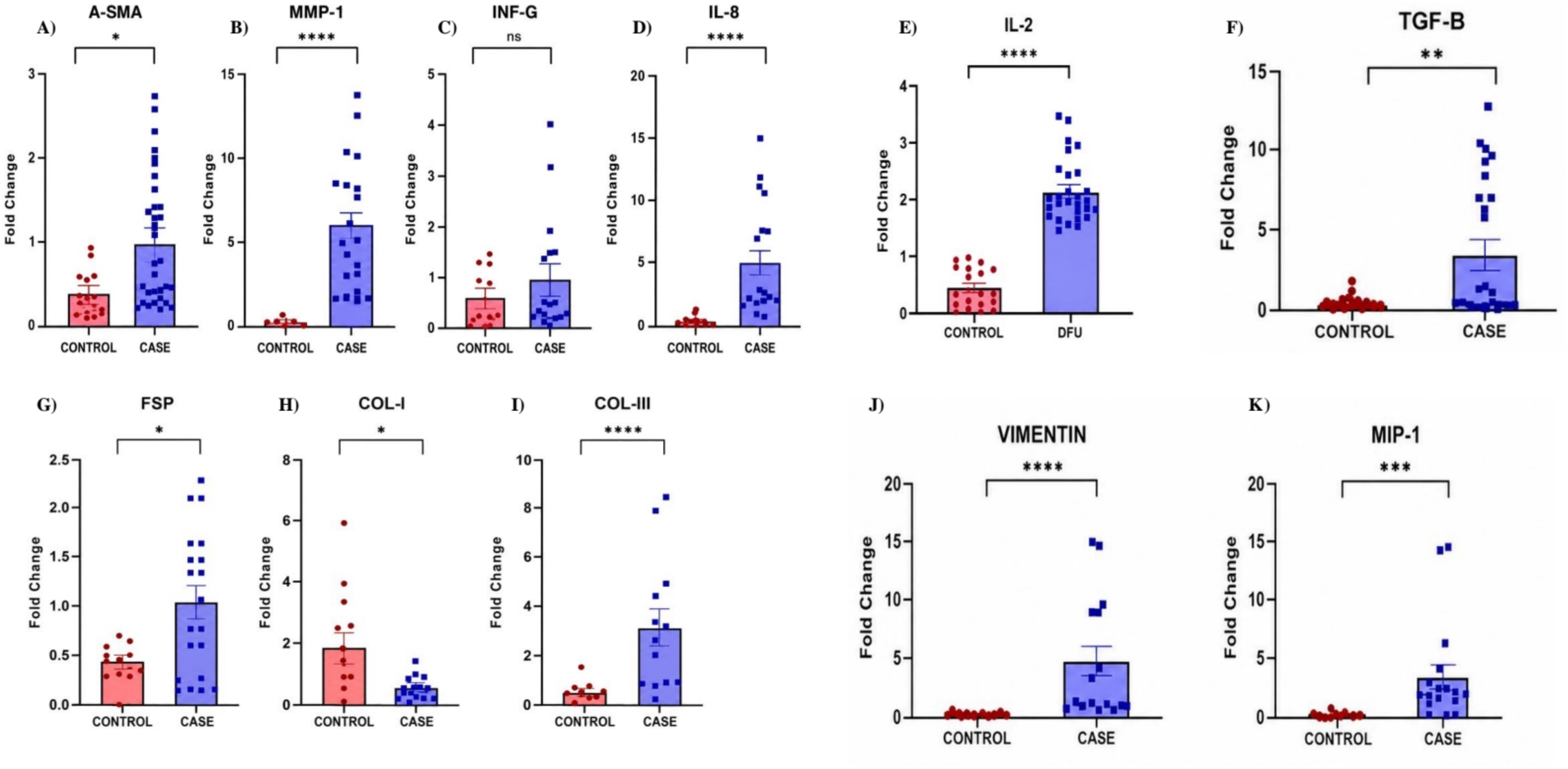


Fig. 17


A)
A-SMA
*
Fold Change
CONTROL
CASE
B)
MMP-1
****
Fold Change
CONTROL
CASE
C)
INF-G
ns
Fold Change
CONTROL
CASE
D)
IL-8
****
Fold Change
CONTROL
CASE
E)
IL-2
****
Fold Change
CONTROL
DFU
F)
TGF-B
**
Fold Change
CONTROL
CASE
G)
FSP
*
Fold Change
CONTROL
CASE
H)
COL-I
*
Fold Change
CONTROL
CASE
I)
COL-III
****
Fold Change
CONTROL
CASE
J)
VIMENTIN
****
Fold Change
CONTROL
CASE
K)
MIP-1
***
Fold Change
CONTROL
CASE

Supplementary Files

This is a list of supplementary files associated with this preprint. Click to download.

- Supplementrytables.docx